ARTICLE

PI4P/PS countertransport by ORP10 at ER–endosome membrane contact sites regulates endosome fission

Asami Kawasaki[1], Akiko Sakai[1], Hiroki Nakanishi[2], Junya Hasegawa[3], Tomohiko Taguchi[4], Junko Sasaki[3], Hiroyuki Arai[4], Takehiko Sasaki[2,3], Michihiro Igarashi[1], and Fubito Nakatsu[1]

Membrane contact sites (MCSs) serve as a zone for nonvesicular lipid transport by oxysterol-binding protein (OSBP)-related proteins (ORPs). ORPs mediate lipid countertransport, in which two distinct lipids are transported counterdirectionally. How such lipid countertransport controls specific biological functions, however, remains elusive. We report that lipid countertransport by ORP10 at ER–endosome MCSs regulates retrograde membrane trafficking. ORP10, together with ORP9 and VAP, formed ER–endosome MCSs in a phosphatidylinositol 4-phosphate (PI4P)-dependent manner. ORP10 exhibited a lipid exchange activity toward its ligands, PI4P and phosphatidylserine (PS), between liposomes in vitro, and between the ER and endosomes in situ. Cell biological analysis demonstrated that ORP10 supplies a pool of PS from the ER, in exchange for PI4P, to endosomes where the PS-binding protein EHD1 is recruited to facilitate endosome fission. Our study highlights a novel lipid exchange at ER–endosome MCSs as a nonenzymatic PI4P-to-PS conversion mechanism that organizes membrane remodeling during retrograde membrane trafficking.

Introduction

Membrane contact sites (MCSs) are sites of direct communication for organelles and the plasma membrane (PM), where two cellular membranes are closely apposed (Scorrano et al., 2019). Accumulating evidence demonstrates that the ER forms MCSs with most of the organelles or the PM in eukaryotes (Bohnert, 2020; Wu et al., 2018). MCSs have been shown to be involved in several functions, including but not limited to Ca²⁺ regulation, lipid metabolism, and signaling (Prinz et al., 2020). In particular, MCSs serve as a zone for nonvesicular lipid transport mediated by so-called lipid transfer proteins (LTPs; Wong et al., 2019). LTPs generally possess a hydrophobic pocket that harbors lipid molecules, and they act as regulators for intracellular lipid distribution by transferring lipids between cellular membranes (Holthuis and Menon, 2014).

Oxysterol-binding protein (OSBP)–related proteins (ORPs) are a class of LTPs that consist of 12 different members in mammals (Raychaudhuri and Prinz, 2010). ORPs have the well-conserved OSBP-related domain (ORD), a ligand-binding pocket that accommodates a lipid ligand (Tong et al., 2016). Studies now show that the repertoire of their ligands has expanded to include

not only oxysterol but also other lipids such as cholesterol, phosphoinositides, phosphatidylserine (PS), or phosphatidylcholine (PC; Balla et al., 2019). Additionally, most ORPs contain a PH domain and an ER localization domain/motif such as a transmembrane domain or the two phenylalanines in acidic tract (FFAT) motif that is recognized by the ER protein vesicle-associated membrane protein (VAMP)–associated protein A (VAPA)/VAPB (Alli-Balogun and Levine, 2019). Via those dual membrane association determinants, ORPs localize at MCSs by simultaneously interacting with the ER and other cellular membranes, and they act as a sensor or transporter of their lipid ligands (Kentala et al., 2016; Pietrangelo and Ridgway, 2018).

A characteristic functional property of ORPs is their lipid countertransport activity. Recent studies suggest that several ORPs harbor two different lipids as their ligands, phosphatidylinositol 4-phosphate (PI4P) as a common ligand or other lipids as another ligand, and mediate counterdirectional transport of those two different lipids (Chung et al., 2015; Mesmin et al., 2013; Sohn et al., 2018; D'Souza et al., 2020). We have shown that ORP5 and ORP8 mediate countertransport of PI4P

[1]Department of Neurochemistry and Molecular Cell Biology, Niigata University School of Medicine and Graduate School of Medical/Dental Sciences, Niigata, Japan; [2]Graduate School of Medicine and Research Center for Biosignal, Akita University, Akita, Japan; [3]Department of Biochemical Pathophysiology, Medical Research Institute, Tokyo Medical and Dental University, Tokyo, Japan; [4]Laboratory of Health Chemistry, Graduate School of Pharmaceutical Sciences, The University of Tokyo, Tokyo, Japan.

Correspondence to Fubito Nakatsu: nakatsu@med.niigata-u.ac.jp; H. Nakanishi's present address is Lipidome Lab Co., Ltd., Akita, Japan; T. Taguchi's present address is Department of Integrative Life Sciences, Graduate School of Life Sciences, Tohoku University, Sendai, Japan.

and PS at the ER–PM MCSs (Chung et al., 2015). This lipid countertransport was driven by a PI4P concentration gradient between the ER and the PM. PI4P is continuously synthesized at the PM, while it is metabolically degraded at the ER. The PI4P concentration gradient determines the direction of its transport to the ER, which in turn facilitates the counterdirectional transport of PS from the ER. Therefore, this mechanism—PI4P-driven lipid countertransport—helps deliver lipids from the ER to other membranes in exchange for PI4P via MCSs (Antonny et al., 2018; Balla et al., 2019; Mesmin and Antonny, 2016).

Despite the fact that the general mechanism of PI4P-driven lipid countertransport has been characterized, cellular function regulated by this mechanism is still largely unknown. In PI4P-driven lipid countertransport, PI4P is passively replaced by ORPs with other lipids that are transported from the ER. This would be a lipid "conversion" that changes a property of a membrane and thus potentially impacts numerous cellular functions. However, which cellular processes directly couple to this lipid conversion event and how cellular processes harness such lipid conversion remain elusive. More specifically, how such exchanged lipid exerts its specific biological function is poorly understood. Answering those questions will reveal the biological significance of PI4P-driven lipid countertransport at MCSs.

In this study, we identified ORP10 as a bona fide lipid exchanger at ER–endosome MCSs. ORP10 localized at the MCSs between the ER and the PI4KIIα-positive endosomes that are tethered by ORP9 and VAP. Both in vitro and in situ, ORP10 mediates exchange of two different lipids, PS and PI4P, the latter of which was identified in this study as a ligand of ORP10. In the cellular context, ORP10 supplied PS in exchange for PI4P to endosomes where the PS-binding protein EHD1 is recruited, thereby promoting the fission process of tubulovesicular carrier from endosomes in the retrograde trafficking pathway. Thus, ORP10 is a new lipid exchanger at ER–endosome MCSs, and ORP10-mediated lipid conversion from PI4P to PS on endosomes controls retrograde membrane trafficking.

Results

ORP10 localizes at a subset of PI4KIIα-positive endosomes

Previous studies demonstrated that PI4P-driven lipid countertransport is supported by continuous PI4P synthesis at the PM or Golgi by PI4KIIIα or PI4KIIIβ, respectively (Chung et al., 2015; Mesmin et al., 2013, 2017; Sohn et al., 2018). However, such lipid countertransport has not been reported at endosomes, which also contain PI4P synthesized by PI4KIIα/β (Balla and Balla, 2006). To identify ORPs that function at the ER–endosome MCSs, we tested ORP family proteins for their ability to localize at endosomes containing Rab5 as well as PI4KIIα, the PI4K that synthesizes PI4P at endosomes (Balla et al., 2002). When expressed at low levels, GFP-tagged ORP10 was found to colocalize with Rab5 or PI4KIIα at endosomes, which are also closely associated with the ER (Fig. 1, A and B; and Fig. S1, A and B). To confirm endogenous localization of ORP10, we generated a HeLa cell line by CRISPR/CRISPR-associated protein 9 (Cas9) in which the endogenous ORP10 is expressed as a 3xHA-tagged form. Western blot analysis showed a single band at the expected size

detected by anti-HA antibody, and this corresponding signal was almost undetectable upon knocking down with the siRNA against ORP10 (Fig. 1 C). Immunofluorescence staining of the ORP10-3xHA knock-in (KI) HeLa cells with anti-HA antibody showed the punctate structures of endogenous ORP10 that colocalized well with PI4KIIα as well as with VAPA, an ER protein (Fig. 1, D and E), consistent with the localization of GFP-ORP10 (Fig. 1, A and B; and Fig. S1, A and B). Intriguingly, however, endogenous ORP10 also colocalized with Rab7 even more than with Rab5 (Fig. 1 E and Fig. S1 C). This is consistent with previous reports showing that PI4KIIα and its metabolic product PI4P localize and function at later endosomal compartments (Baba et al., 2019; Hammond et al., 2014). On the other hand, ORP10 colocalized less with Sac2/INPP5F[D460A], an endosomal PI4P phosphatase (Hsu et al., 2015; Nakatsu et al., 2015; we used a phosphatase-dead D460A mutant, which shows less cytosolic localization; Fig. S1 C). These results demonstrate that ORP10 localizes at endosomes and more so at the later compartments.

PI4P-dependent localization of ORP10 at endosomes via its PH domain

To investigate how ORP10 localizes at endosomes, we tested ORP10 mutants (Fig. 1 F) for their localization. Pleckstrin homology (PH) domains mediate membrane targeting of various proteins, including ORPs (Lemmon, 2008). In fact, the PH domain of ORP10 (PH) sufficiently localized at the PI4KIIα-positive endosomes similar to full-length WT (Full; Fig. 1 G). In contrast, neither a deletion mutant lacking a PH domain (ΔPH) nor a construct harboring the N-terminal region before the PH domain (N-term) showed such endosomal localization (Fig. 1 G). These results indicate that the PH domain of ORP10 determines its endosomal localization. We next examined whether the localization of the ORP10 PH domain requires phosphoinositides, as is the case for other ORPs. We took advantage of the rapamycin-mediated FK506-binding protein (FKBP)/FKBP12-rapamycin-binding (FRB) domain dimerization system to acutely deplete phosphatidylinositol 3-phosphate (PI3P) or PI4P, the major phosphoinositides at endosomes, and then tested its effect on the localization of the ORP10 PH domain (2xPH[ORP10]). To dephosphorylate PI3P or PI4P, we used FKBP fusion with the PI3P phosphatase MTM1 (FKBP-MTM1; Blondeau et al., 2000) or the Sac1 domain from Sac2/INPP5F (FKBP-Sac1d[Sac2/INPP5F]), respectively. As previously reported, these constructs successfully depleted PI3P or PI4P monitored by a 2xFyve domain from HRS (2xFyve[HRS]; Gillooly et al., 2000) or a PH domain from OSBP (PH[OSBP]; Levine and Munro, 2002), respectively (Fig. S1, D–G; Nguyen et al., 2019; Hammond et al., 2014). 2xPH[ORP10] was quickly delocalized from endosomes by acute depletion of PI4P, but not PI3P, to a similar extent as PH[OSBP] (Fig. 1, H–J; and Fig. S1, D and E), indicating a strong dependency of its endosomal localization on PI4P. This is consistent with a previous finding showing that the recombinant ORP10 PH protein recognizes PI4P on a membrane strip (Nissilä et al., 2012). Consistently, full-length ORP10 was also quickly delocalized from Rab7-positive endosomes upon PI4P depletion (Fig. S1, H and I). These results demonstrate that the endosomal localization of ORP10 via its PH domain depends on PI4P.
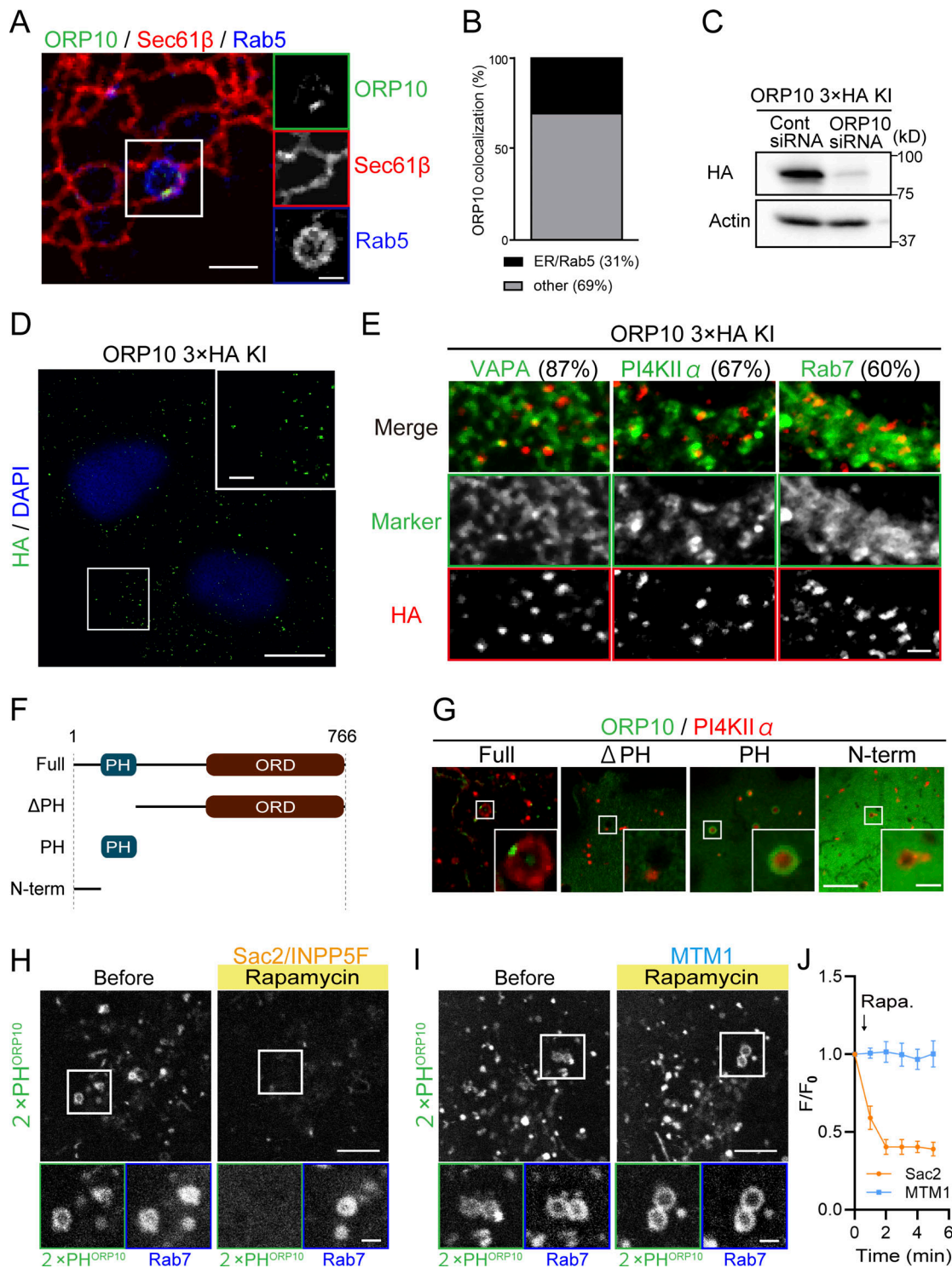
Kawasaki et al.
Lipid exchange by ORP10 regulates endosome fission

Journal of Cell Biology
https://doi.org/10.1083/jcb.202103141

2 of 19

Figure 1. **PI4P-dependent localization of ORP10 at endosome via its PH domain. (A)** Confocal images of Cos7 cell expressing GFP-ORP10, RFP-Sec61β, and iRFP-Rab5. Scale bars, 2.5 μm (full size) and 1 μm (inset). **(B)** Quantification of A showing the percentage of ORP10 colocalized with Rab5 and Sec61β (*n* = 11 cells). **(C)** Western blotting of ORP10-3xHA KI HeLa cells transfected with siRNA for control (Cont) or ORP10. **(D)** Immunofluorescence staining of endogenous ORP10-3xHA with anti-HA antibody in ORP10-3xHA KI cells showing endosome-like punctate structures. Scale bars, 10 μm (full size) and 2 μm (inset). **(E)** Colocalization of endogenous ORP10 (ORP10-3xHA) with VAPA (AcGFP-VAPA), PI4KIIα (antibody), or Rab7 (GFP-Rab7A) and its quantification (percentage colocalization; n ≥ 10 cells). Scale bar, 1 μm. **(F)** Schematic of ORP10 constructs (Full [1–766], ΔPH [182–766], PH [77–173], or N-term [1–76]) used in G. Blue or brown box indicates the PH domain or ORD, respectively. **(G)** Confocal images of Cos7 cells expressing GFP-tagged ORP10 constructs and mScarlet-PI4KIIα. Scale bars, 5 μm (full size) and 1 μm (inset). **(H–J)** Representative images showing endosomal localization of ORP10 PH domain (2xPH^ORP10) before (0 min) or after (5 min) recruitment of FKBP fused with Sac1 domain from Sac2/INPP5F (H) or MTM1 (I) by Rab7-FRB and its kinetics (J; mean ± SEM; *n* = 11 cells for Sac2/INPP5F and MTM1). Scale bars, 5 μm (full size) and 1 μm (inset). Rapa., rapamycin.

ORP10 localizes at ER–endosome MCSs tethered by VAPA and ORP9

Most ORPs anchor to the ER by a transmembrane domain or an FFAT motif recognized by an ER protein VAPA or VAPB (Loewen et al., 2003). However, ORP10 seemed to have neither of these upon inspection of its amino acid sequence. Nevertheless, ORP10 was well associated with the ER (Fig. 1, A and E), strongly suggesting that ORP10 may localize at the MCSs between the ER and the PI4KIIα-positive endosomes. To find a clue for how ORP10 localizes at the ER–endosome MCSs, we took a proteomic approach to identify a binding partner of ORP10. Parental or ORP10-3xHA KI HeLa cells were subjected to immunoprecipitation with anti-HA antibody followed by mass spectrometry (MS). Analysis of the proteins specifically detected in the immunoprecipitates from the ORP10-3xHA KI cells revealed another member of the ORP family, ORP9, as a top hit (Fig. 2 A). Western blot analysis of HA immunoprecipitates using ORP9-specific antibody confirmed the interaction of ORP10 with ORP9 (Fig. 2 B), consistent with a previous study (Nissilä et al., 2012). To map which region of ORP10 binds ORP9, coimmunoprecipitation was performed using ORP10 mutants (Fig. 2 C). HA-ORP9 pulled down full-length (Full), ΔORD, or ΔPH, but not the PH domain of ORP10 (PH), indicating that ORP10 associated with ORP9 in its linker region between the PH domain and ORD (Fig. 2, C–E).

Given the presence of a functional FFAT motif in ORP9 (Fig. 2 D; Wyles and Ridgway, 2004), ORP10, ORP9, and VAP may form an ER–endosome MCS. As expected, ORP10 substantially colocalized with ORP9 at endosomes that were also positive for VAPA (Fig. 2, F and G), indicating that ORP10 localized at the MCSs tethered by ORP9 and VAP. We then tested whether the localization of ORP10 at the MCSs depends on ORP9 as well as VAPs. We generated ORP9 KO HeLa cells by CRISPR/Cas9 (Fig. 2 H) and examined the localization of ORP10. Association of ORP10 with the ER was almost lost in ORP9 KO cells, with a few punctate signals seen occasionally at peripheral regions at the steady state (Fig. 2, I and J), suggesting that ORP9 is required for the localization of ORP10 at the ER–endosome MCSs. This also supports the absence of the FFAT motif in ORP10 because it was not able to localize at the MCSs in the absence of ORP9. Consistent with previous reports showing the interaction of ORP9 with VAP via its FFAT motif (Wyles and Ridgway, 2004), VAPA/VAPB knockdown (KD) also affected ORP10 localization at the MCSs (Fig. S1, J–L). These results demonstrate that the localization of ORP10 at the ER–endosome MCSs depends on ORP9 as well as VAPs.

Most notably, several lines of evidence revealed an exclusive localization of ORP10 at the ER–endosome MCSs (Fig. 1, A and E; Fig. S1 B; Fig. 2, F–J; and Fig. S1, J–L). Thus, delocalization of full-length ORP10 by PI4P depletion (Fig. S1, H and I) also indicates a PI4P dependency for its localization at the MCSs. Taking all these data into consideration, we conclude that both PI4P and ORP9 are required for the localization of ORP10 at ER–endosome MCSs.

Identification of PI4P as a novel ligand of ORP10

We next sought to investigate whether ORP10 mediates countertransport of lipids. A previous study demonstrated that

ORD^{ORP10} binds PS in vitro (Maeda et al., 2013). Considering that ORPs are suggested to have potentially two different ligands—PI4P as a common driver ligand and other lipids as a second cargo ligand (Antonny et al., 2018; Tong et al., 2016, 2013)—ORP10 could accommodate PI4P in addition to PS. Therefore, we tried to identify the phosphoinositide sequestered in the ORD^{ORP10} using a strategy with which we have successfully identified the ligands of ORP8 (Chung et al., 2015). MS analysis of 3xFlag-tagged ORD^{ORP10} purified from Expi293F suspension cells identified a candidate ligand PI4P as the most concentrated phosphoinositide (Fig. 3, A and B; and Fig. S2 A).

ORP10 mediates countertransport of PI4P and PS between liposomes

These findings prompted us to investigate the transport activity of ORP10 toward its ligands, PI4P and PS. To this end, we performed an in vitro lipid transport assay using liposomes as model membranes (Moser von Filseck et al., 2015). To assess the transport of lipids, donor liposomes containing either PS or PI4P as well as rhodamine-phosphatidylethanolamine (Rhod-PE) and acceptor liposomes were mixed with an NBD-conjugated lipid sensor. The fluorescence from NBD was continuously measured upon addition of ORD by a microplate reader to monitor lipid transport. When a lipid sensor binds to donor liposomes, NBD fluorescence is quenched due to fluorescence resonance energy transfer with Rhod-PE. If lipids are transported to acceptor liposomes by ORD, a lipid sensor changes its position from donor to acceptor liposomes, where NBD fluorescence increases due to dequenching. Therefore, an increase in NBD fluorescence reflects the transport of lipids from donor to acceptor liposomes (Fig. 3, C and D).

As a control experiment, we first tested the ORD of ORP8 (ORD^{ORP8}; Fig. S2 B), which has been demonstrated to mediate countertransport of PI4P and PS (Chung et al., 2015). Addition of ORD^{ORP8} induced a slight increase in the transport of PS to acceptor liposomes containing only PC (Fig. S2 C). However, such transport was enhanced when PI4P was present in the acceptor liposomes (Fig. 3 E and Fig. S2 C). Similarly, the transport of PI4P was significantly enhanced when acceptor liposomes contained PS (Fig. 3 F and Fig. S2 D). These results are consistent with previous reports and also suggest a "countertransport" activity of ORP8, in which the transport of one lipid is promoted by counterdirectional transport of another lipid (Chung et al., 2015; Ghai et al., 2017). In the case of ORP10, the transport of PS by ORD^{ORP10} to a donor liposome containing only PC was minimal, while that to donor liposomes containing PI4P was significantly enhanced (Fig. 3 E; and Fig. S2, E and F). Likewise, the transport of PI4P was enhanced when acceptor liposomes contained the other ligand, PS (Fig. 3 F and Fig. S2 G). These results clearly demonstrate that ORP10 is able to transport PI4P and PS between liposomes. Furthermore, the enhancement of the transport of a lipid by the presence of another lipid in acceptor liposomes, which is indicative of countertransport activity by ORD^{ORP10}, as was the case for ORD^{ORP8} (Fig. 3, E and F), suggests a possible role of ORP10 as a lipid exchanger.
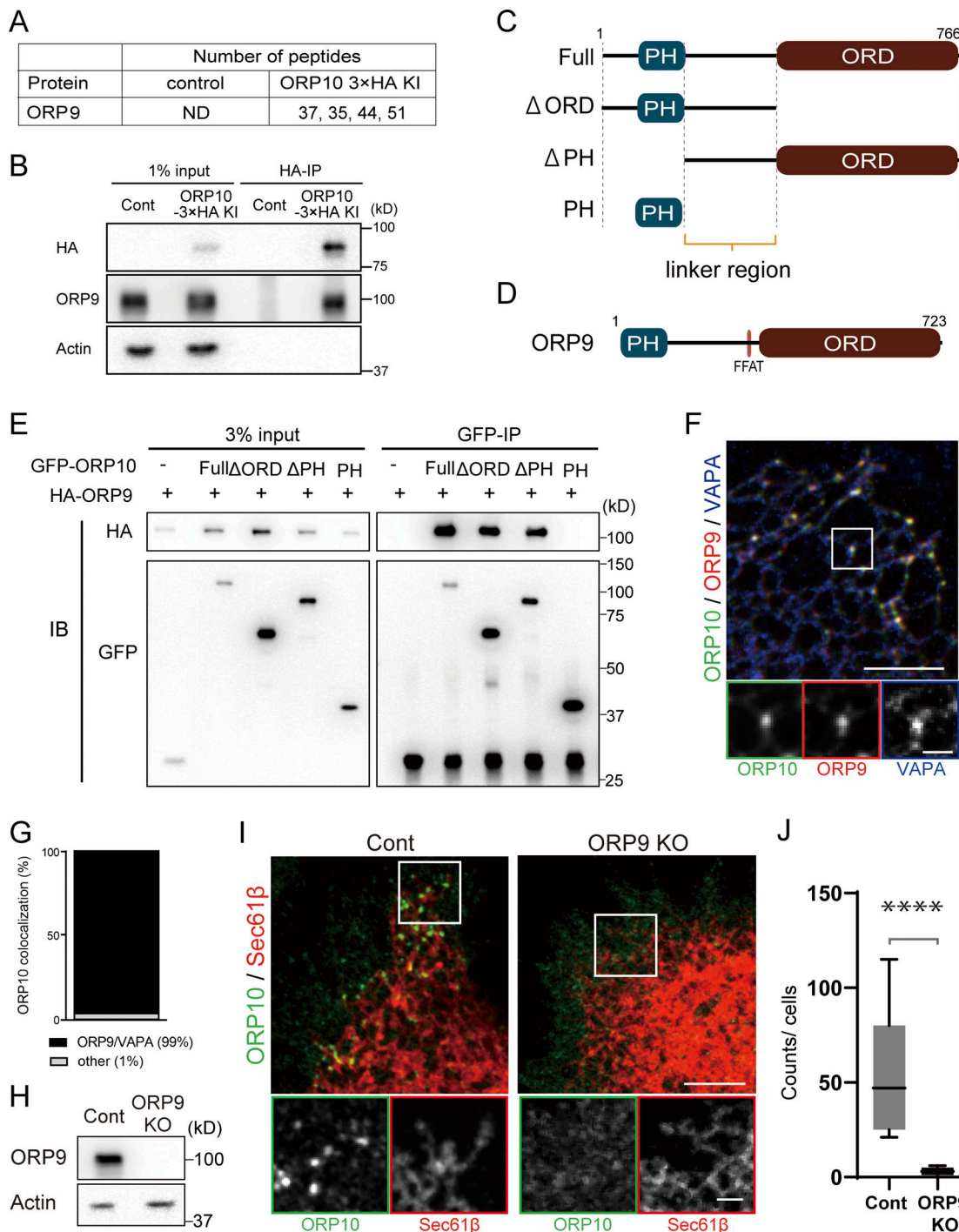
Figure 2. **ORP10 associates and colocalizes with ORP9 at ER–endosome MCSs. (A)** ORP9 as an ORP10-binding protein revealed by MS of ORP10-3xHA immunoprecipitates. The number of ORP9 peptides detected from parental control (Cont) or ORP10-3xHA KI cells is shown. ND, not detected. **(B)** Parental or ORP10-3×HA KI HeLa cells were lysed and subjected to immunoprecipitation (IP) using anti-HA antibody followed by Western blotting with HA, ORP9, or actin antibody. **(C and D)** Schematic of ORP10 (C) and ORP9 (D) constructs used in E. Blue, brown, or pink box indicates the PH domain, ORD, or FFAT motif, respectively. **(E)** GFP, GFP-ORP10 (FL), GFP-ORP10$^{\Delta ORD}$ (ΔORD), GFP-ORP10$^{\Delta PH}$ (ΔPH), or GFP-PH^{ORP10} (PH) was coexpressed with HA-ORP9 in HEK293T cells, lysed, and subjected to immunoprecipitation using anti-GFP antibody, followed by Western blotting (IB) with antibodies as indicated. **(F and G)** Cos7 cells expressing GFP-ORP10, mCherry-ORP9, and BFP-VAPA (F) and its quantification for colocalization with ORP10 (G; n = 11 cells). Scale bars, 5 µm (full size) and 1 µm (inset). **(H)** Western blotting of control or ORP9 KO cells using antibodies indicated. **(I and J)** Representative images showing endosomal localization of GFP-ORP10 and its association with the ER (mRFP-Sec61β) in control (Cont) or ORP9 KO cells (I) and its quantification (number of ORP10-positive endosomes associated with the ER per cell; J; n ≥ 11 cells). Scale bars, 5 µm (full size) and 1 µm (inset). ****, P < 0.0001.
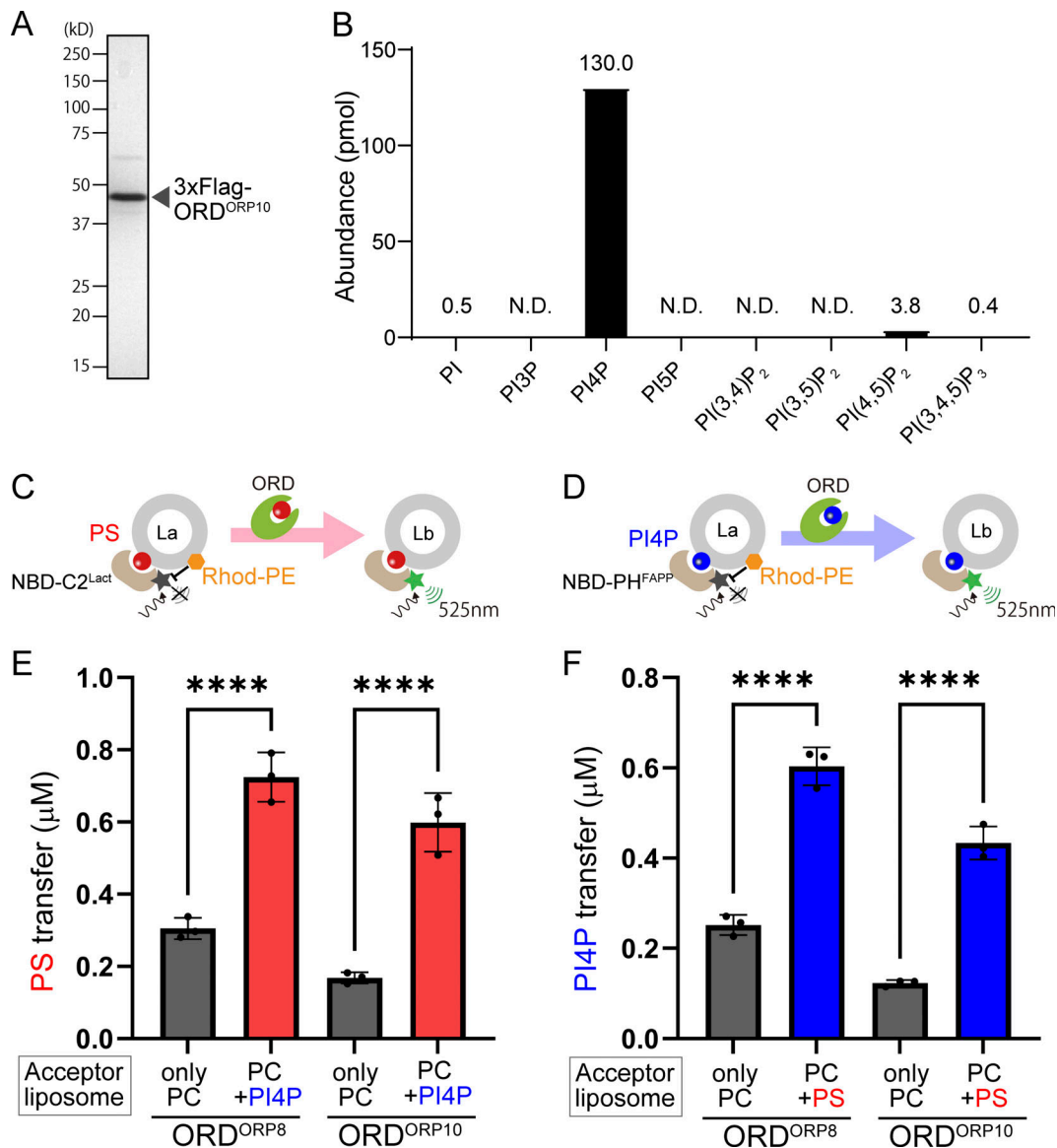
Figure 3. **ORD^{ORP10} mediates countertransport of P4P and PS between liposomes. (A)** Coomassie Brilliant Blue–stained SDS-PAGE gel of 3xFlag-ORD^{ORP10} proteins purified from Expi293F cells. **(B)** Phosphoinositide (PI) species detected by MS of 3xFlag-ORD^{ORP10} proteins purified from Expi293F cells. N.D., not detected. **(C and D)** Schematic representation for in vitro lipid transport assay for PS (C) or PI4P (D). A PH domain from FAPP1 (NBD-PH^{FAPP}; Balla et al., 2005) or a C2 domain from lactadherin (NBD-C2^{Lact}; Yeung et al., 2008) was used as a sensor for PI4P or PS, respectively. **(E)** The amount of PS (μM) transported to acceptor liposomes containing only PC (gray) or PC + PI4P (red) by ORD^{ORP8} (left) or ORD^{ORP10} (right; mean ± SD; n = 3 independent experiments). **(F)** The amount of PI4P (μM) transported to acceptor liposomes containing only PC (gray) or PC + PS (blue) by ORD^{ORP8} (left) or ORD^{ORP10} (right; mean ± SD; n = 3 independent experiments). ****, P < 0.0001.

PI4P/PS countertransport at ER–endosome MCSs by ORP10 underlies a PI4P-to-PS conversion on endosomes

We then examined whether ORP10, like ORP5/ORP8, mediates countertransport of those lipids in the cellular context. As a gain-of-function approach, we set up a lipid countertransport monitoring assay where ORD^{ORP10} is acutely recruited to the ER–endosome MCSs (Fig. 4 A). ORD^{ORP10} fused to FKBP (FKBP-ORD^{ORP10}) was expressed along with VAPA and ORP9-ΔORD-FRB. Upon addition of rapamycin, FKBP-ORD^{ORP10} was acutely recruited from the cytosol to the ER–endosome MCSs tethered by VAPA and ORP9-ΔORD-FRB (Fig. S3, A and B). When we monitored the levels of PI4P and PS at endosomes by their

specific markers (PH^{OSBP} [Levine and Munro, 2002] or C2^{Lact} [Yeung et al., 2008]), the PI4P levels gradually decreased, while the PS levels increased (Fig. 4, B and C). These results suggest that PI4P and PS were exchanged by ORD^{ORP10} between the ER and endosomes in situ.

A similar lipid countertransport activity between ORP10 and ORP8 seen in the in vitro lipid transport assay (Fig. 3, E and F) indicates that ORP10-mediated lipid exchange could be countertransport driven by PI4P. Therefore, we next tested whether PI4P drives PS transport by ORP10 through lipid exchange. Tandem histidines in the lipid-binding motif "EQVSHHPP" in ORD are conserved in all ORP/Osh family proteins
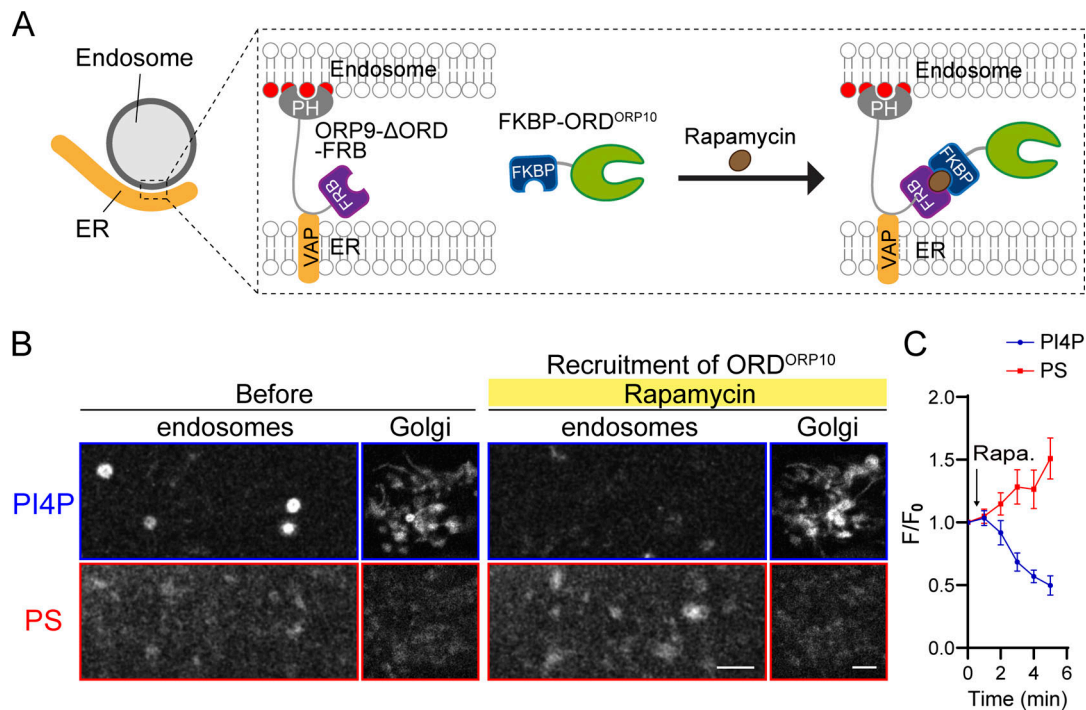
Figure 4. ORD^ORP10 mediates countertransport of P4P and PS at ER–endosome MCSs. (A) Cartoon illustrating the principle of lipid exchange assay in cultured cells. Addition of rapamycin acutely recruits FKBP-ORD^ORP10 to the ER–endosome MCSs tethered by ORP9-ΔORD-FRB. **(B)** Representative snapshot images of confocal live microscopy showing PI4P levels (GFP-OSBP-PH) or PS levels (mRFP-LactC2) before (0 min) and after (5 min) acute recruitment of ORD^ORP10 to ER–endosome MCSs. Note that the PI4P levels in the Golgi did not change after acute recruitment of ORD^ORP10. Scale bars, 5 μm (full size) and 1 μm (inset). **(C)** Quantification for (B; grand mean ±SEM; n = 11 cells). Note that rapamycin (Rapa.) was added at 1 min.

(Raychaudhuri and Prinz, 2010). These histidine residues have been shown to be responsible for PI4P binding (de Saint-Jean et al., 2011; Tong et al., 2013). Therefore, we used the ORP10 ORD-bearing mutations in the corresponding histidines (ORD^ORP10-HH/AA) to perform the exchange assay. Acute recruitment of FKBP-ORD^ORP10-HH/AA did not decrease, but rather increased, PI4P levels at endosomes (Fig. S3, C and D), suggesting that the ORP10 HH/AA mutant was unable to transfer PI4P from endosomes to the ER as expected. (Note that this increase in endosomal PI4P upon recruitment of ORD^ORP10-HH/AA indicates that the PI4P transport via ER–endosome MCSs lessens the accumulation of this lipid at endosomes, as has been demonstrated in OSBP/VAP null cells; Dong et al., 2016.) In this situation, the endosomal PS levels did not increase (Fig. S3, C and D), indicating that PS was not countertransported to endosomes. This is in sharp contrast to the increase of PS, which indicates the occurrence of PS countertransport, upon recruitment of WT ORD (Fig. 4, B and C). These data indicate that PI4P transport by ORP10-ORD does drive the counterdirectional transport of PS from the ER to endosomes. These results also suggest that this lipid exchange by ORP10 functioned as a PI4P-to-PS conversion on endosomes where a pool of PI4P is replaced with PS.

To examine the role of ORP10-mediated lipid countertransport in cell physiology, we established ORP10 knockout (KO) cells by CRISPR/Cas9. Western blotting confirmed that ORP10 was undetectable while ORP9 was unchanged in KO cells (Fig. 5 A). Then we investigated the levels of PS and PI4P at endosomes.

This loss-of-function approach demonstrated that the amount of endosomal PS in ORP10 KO cells was less than that in control cells, further indicating that ORP10 mediates countertransport of PS from the ER to endosomes (Fig. 5 B, upper). Contrary to our prediction, however, endosomal PI4P levels did not increase in KO cells (Fig. 5 B, lower). This is likely due to compensation by ORP9, as it has been suggested that one of its ligands is PI4P (Liu and Ridgway, 2014), although its lipid exchange function has not been proved. Indeed, ORP9 depletion, which also leads to a loss of lipid exchange function of ORP10 due to its mislocalization at the MCSs (Fig. 2, I and J), caused an increase in PI4P at endosomes (Fig. 5 B), suggesting a compensatory PI4P transport by ORP9 in the absence of ORP10. In contrast, endosomal PS levels in ORP9 KO cells were lower than in control cells, and the reduction was only slightly further enhanced from, but almost comparable to, that seen in ORP10 KO cells (Fig. 5 B). These results suggest a role of ORP10 in supplying endosomes with PS via its lipid exchange activity.

We examined the role of ORP10 further by rescue experiment (Fig. 5 C). The endosomal PS levels in ORP10 KO cells were reversed to control levels by WT ORP10, but not by ORP9, suggesting that ORP10 is responsible for the PS defects. Furthermore, neither ORP10^ΔPH nor ORP10^ΔORD mutant fully rescued such defects. These results suggest that PI4P-mediated localization at the MCSs, as well as lipid exchange activity of ORP10, is required to maintain proper levels of PS at endosomes. Based on these results, we conclude that ORP10 supplies a pool of PS to endosomes in exchange for PI4P.
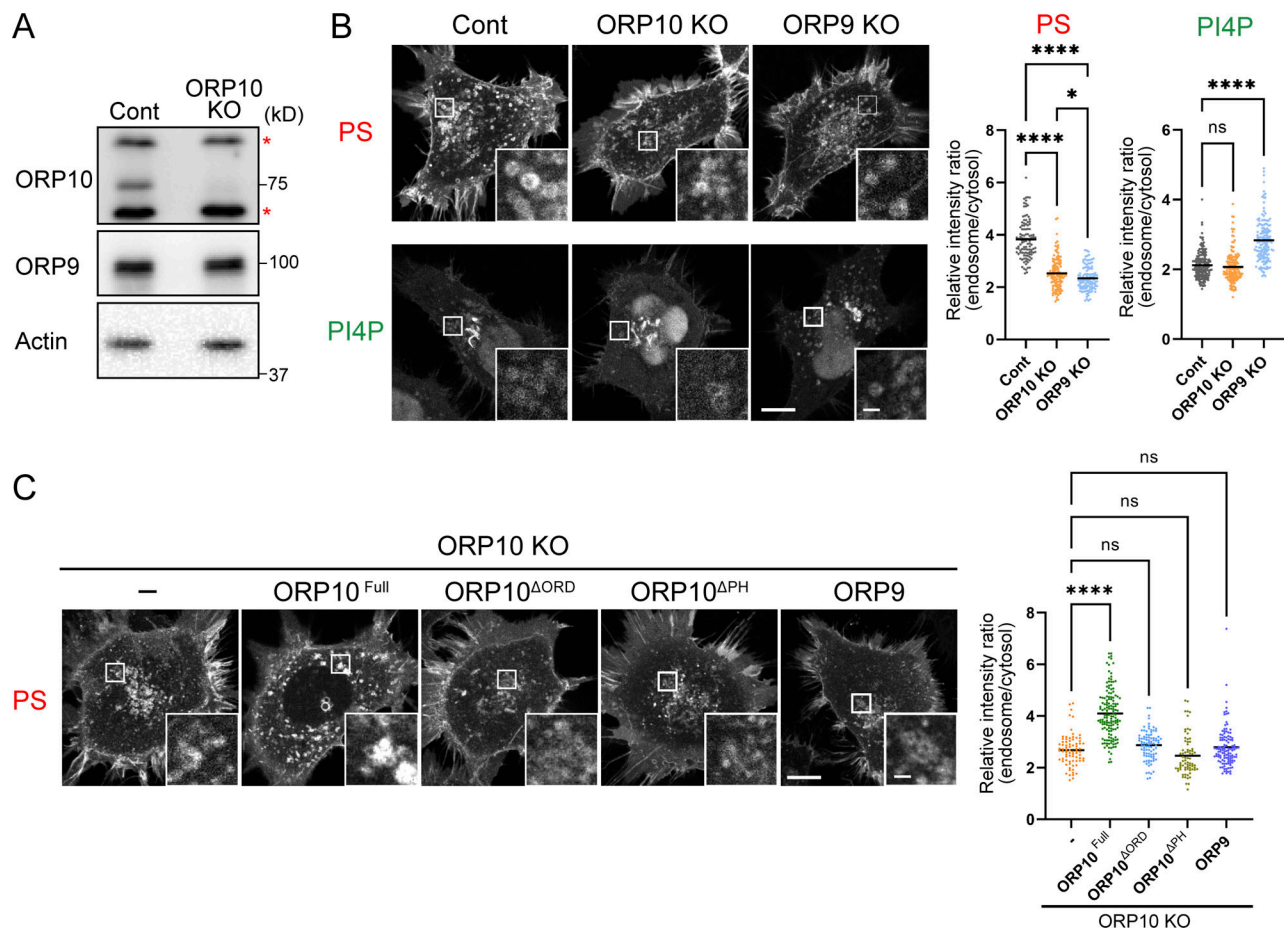
Figure 5. **Reduction of endosome PS in the absence of ORP10. (A)** Western blotting of whole-cell lysates from control (Cont) or ORP10 KO cells with the antibodies indicated. Asterisks indicate nonspecific bands. **(B)** Confocal microscopic images and their quantification for PS levels (mRFP-LactC2; upper) and PI4P levels (GFP-OSBP-PH; lower) of endosomes in control, ORP10 KO, or ORP9 KO cells (mean ± SEM, the number of endosomes for PS quantification; $n = 136$ from 11 cells for control, $n = 131$ from 17 cells for ORP10 KO, $n = 112$ from 13 cells for ORP9 KO, the number of endosomes for PI4P quantification; $n = 168$ from 20 cells for control, $n = 157$ from 21 cells for ORP10 KO, $n = 149$ from 17 cells for ORP9 KO). Scale bars, 10 µm (full size) and 1 µm (inset). **(C)** Confocal microscopic images and their quantification of endosomal PS levels in ORP10 KO cells rescued by reexpression of GFP (−), GFP fused to full-length ORP10 (ORP10^{Full}), ΔORD (ORP10$^{\Delta ORD}$), ΔPH (ORP10$^{\Delta PH}$), or ORP9 (mean ± SEM, the number of endosomes for PS quantification; $n = 78$ from 35 cells for GFP, $n = 145$ from 17 cells for ORP10^{Full}, $n = 90$ from 11 cells for ORP10$^{\Delta ORD}$, $n = 73$ from 10 cells for ORP10$^{\Delta PH}$, $n = 120$ from 12 cells for ORP9). Scale bars, 10 µm (full size) and 1 µm (inset). *, $P < 0.05$; ****, $P < 0.0001$.

Retrograde trafficking of mannose 6-phosphate receptor (M6PR) is delayed in the absence of ORP10

How does this lipid exchange event at ER–endosome MCSs physiologically contribute to cellular processes? A major function of endosomes is as a sorting hub for cargo transport (Huotari and Helenius, 2011; Mellman, 1996). Retrograde transport to the TGN is a trafficking pathway tightly controlled by regulatory proteins and lipids in space and time (Bonifacino and Rojas, 2006). Importantly, ER–endosome MCSs have been shown to control this process (Allison et al., 2017; Hoyer et al., 2018; Rowland et al., 2014), but the underlying mechanism is incompletely understood. We therefore tested whether the retrograde trafficking of cation-independent (CI) M6PR, a well-known cargo for retrograde trafficking (Arighi et al., 2004), is affected in ORP10 KO cells. Tac-M6PR, a chimera of IL-2 receptor fused to the cytoplasmic tail of M6PR, is transported from the PM to the TGN via endosomes. This retrograde transport was monitored by the uptake of anti-Tac antibody fed into the culture media. Most of the anti-Tac antibody reached the TGN in control cells during a 1-h incubation, whereas the amount of antibody left behind at endosomes was higher in ORP10 KO cells (Fig. 6). These results indicate that the retrograde trafficking process was delayed in the KO cells.

Loss of ORP10-mediated lipid countertransport leads to mislocalization of EHD1

A reduction of PS, albeit with normal PI4P levels, at endosomes in ORP10 KO cells (Fig. 5 B) clearly points to a physiological contribution of ORP10-mediated lipid countertransport in providing PS to endosomes. In the retrograde trafficking process, several regulators, including the retromer complex, sorting nexin (SNX)–Bin/Amphiphysin/Rvs (BAR) proteins, the Wiskott-Aldrich syndrome protein and SCAR homolog (WASH) complex, actin, and fission machineries, are coordinated to complete this process (Burd and Cullen, 2014; Cullen and Steinberg, 2018; Derivery et al., 2009; Gautreau et al., 2014;
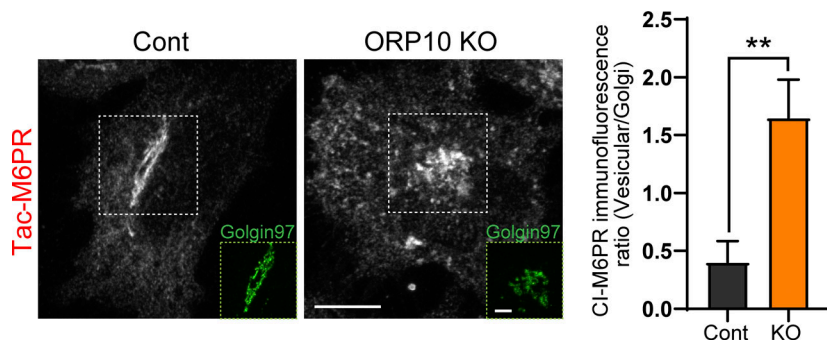
Figure 6. **M6PR retrograde trafficking to TGN is delayed in ORP10 KO cells.** Left: Control (Cont) or ORP10 KO cells expressing Tac-M6PR were incubated with anti-Tac antibody for 60 min to monitor retrograde trafficking to the TGN, followed by immunofluorescence staining with golgin 97 antibody. Right: Graph shows quantification of Tac-M6PR immunofluorescence ratio (vesicular/Golgi; mean ± SEM, n ≥ 6). Scale bars, 10 µm (full size) and 2 µm (inset). **, P < 0.01.

Gomez and Billadeau, 2009; Puthenveedu et al., 2010; Seaman, 2012). Because endosomal PS levels were reduced in ORP10 KO cells, recruitment of such regulators by this lipid would be affected. A candidate is EHD1, a member of the EHD family of proteins that regulate membrane trafficking in the endocytic pathway as ATPases (Grant and Caplan, 2008; Naslavsky and Caplan, 2011). EHD1 has been shown to control membrane remodeling at endosomes (Cullen and Steinberg, 2018; Lee et al., 2015; McKenzie et al., 2012; Seaman, 2012). In particular, EHD1, as a dynamin-like ATPase, has been reported to facilitate the fission process of tubulovesicular carriers from endosomes (Deo et al., 2018; Kamerkar et al., 2019; Seaman, 2012). Importantly, a previous study demonstrated that EHD1 is recruited to endosomes via its PS-binding property (Lee et al., 2015). Thus, we asked whether EHD1 is properly recruited to endosomes in ORP10 KO cells. The recruitment of EHD1 at the endosomes containing SNX1, a component of SNX-BAR proteins, was less than that seen in control cells (Fig. 7, A and B; and Fig. S4, A and B). Notably, localization of SNX1 or other regulatory proteins such as VPS35 (a subunit of the retromer complex) and FAM21 (a subunit of the WASH complex), as well as actin at endosomes, was not overtly changed in KO cells (Fig. S4, C–F).

ORP10-mediated lipid countertransport controls endosome fission

Given the functional property of EHD1 as a fission regulator at endosomes (Cullen and Steinberg, 2018; Deo et al., 2018; Kamerkar et al., 2019; Seaman, 2012), we hypothesized that reduction of EHD1 recruitment caused a fission defect in ORP10 KO cells. To directly test this idea, we performed time-lapse analysis of GFP-tagged SNX1, aiming to monitor the fission process from endosomes. Consistent with the functional property as a fission regulator, EHD1 KD delayed the fission of SNX1-positive tubulovesicular structures from endosomes (Fig. S4, G and H). Next, we examined the effect of the loss of function of ORP10. Compared with the control cells showing a completed fission process by ~10 s, on average, that in ORP10 KO cells took longer (Fig. 7, C and D; and Videos 1 and 2). This delay was rescued by reexpression of WT ORP10, but not by ORP10^ΔORD or ORP9 (Fig. 7 D). These results indicate that PS transport by ORP10-mediated lipid exchange is required for endosome fission and thus reveal a malfunction of the fission process from endosomes due, at least in part, to mislocalization of EHD1 in ORP10 KO cells.

Accordingly, endogenous M6PR was accumulated at the EEA1-positive endosomes in ORP10 KO cells compared with the control cells (Fig. 8, A and B), consistent with the fission defect in ORP10 KO cells. This M6PR accumulation was rescued by WT ORP10, but not by ORP10^ΔORD or ORP9 (Fig. 8, A and B), suggesting that lipid exchange activity of ORP10 is responsible for proper M6PR trafficking. These data demonstrate that ORP10 controls the retrograde trafficking of M6PR at the fission step via its lipid countertransport function.

Discussion

ORP10 is a bona fide lipid exchanger at ER–endosome MCSs

Levels of PI4P are kept low at the ER by a PI4P phosphatase, while other membranes, such as the PM, Golgi, or endosomes/lysosomes, have higher levels due to continuous synthesis of PI4P by PI4KIIIα, PI4KIIIβ, or PI4KIIα/β, respectively (Balla and Balla, 2006; Burke, 2018; Del Bel and Brill, 2018). This spatial regulation of PI4P metabolism generates a PI4P concentration gradient between the ER and other membranes containing PI4P. The PI4P concentration gradient drives lipid countertransport at MCSs as a driving force, and some ORPs operate this lipid countertransport (Antonny et al., 2018; Balla et al., 2019; Lipp et al., 2020). For instance, ORP5/ORP8 or OSBP has been shown to mediate countertransport of PI4P/PS at ER–PM MCSs or PI4P/cholesterol at ER–Golgi MCSs, respectively (Chung et al., 2015; Mesmin et al., 2013). In this lipid countertransport mechanism, PI4P is transported by ORPs along its concentration gradient to the ER, which in turn facilitates the counterdirectional transport of other lipids from the ER. To operate such PI4P-driven lipid countertransport, ORPs are expected to retain the following functional properties. First, ORPs bind PI4P-positive membranes, which secures a gradient of PI4P between two apposed membranes. Second, ORPs associate with the ER so that they bridge the ER and the PI4P-positive membranes. Third, ORPs accommodate and exchange PI4P and other lipids. Given the conservation of the determinants that enable those functions in the ORP family, ORPs could be considered to be lipid exchangers at MCSs. However, only some but not all ORPs have been shown to be lipid exchangers (Lipp et al., 2020; Nakatsu and Kawasaki, 2021). In this study, we showed that ORP10 localizes at ER–endosome MCSs, where it mediates PI4P/PS exchange. First, ORP10 binds PI4P-positive endosomes via its PH domain. Second, ORP10 associates with the ER by interacting with ORP9, which has an FFAT motif that is recognized by ER proteins called
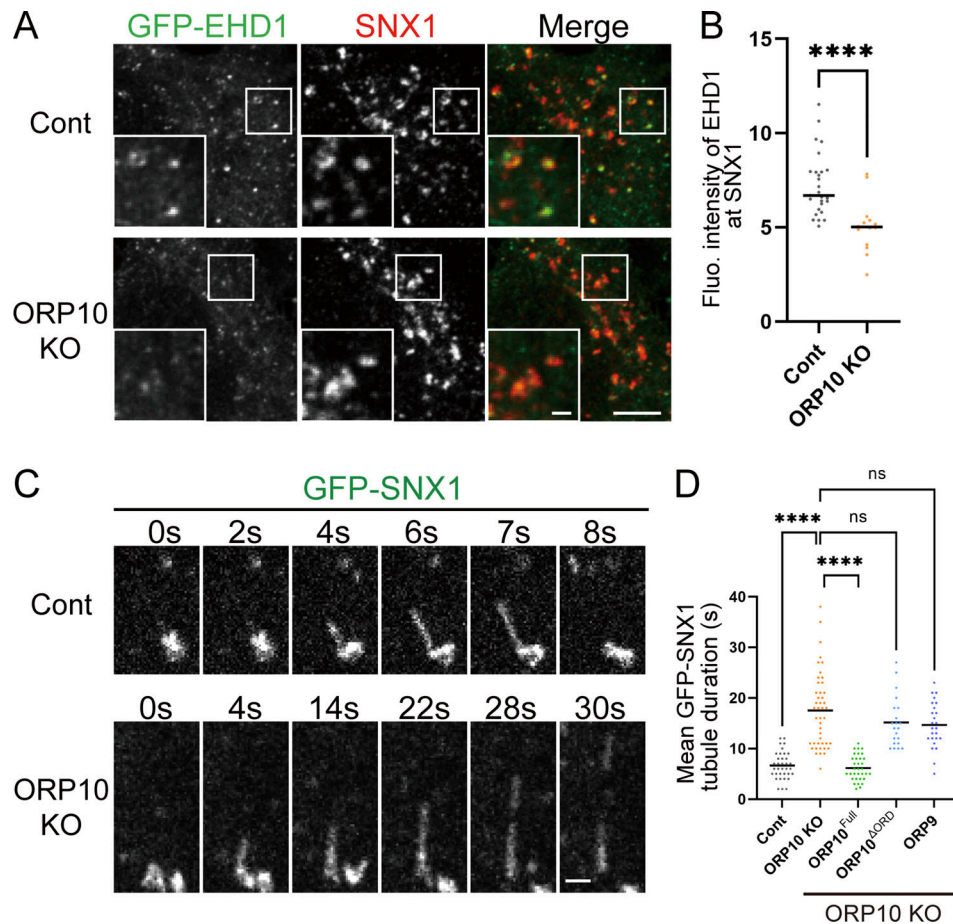
Figure 7. **Endosome fission defect due to reduction of EHD1 recruitment to endosomes in ORP10 KO cells. (A)** Confocal microscopic images of control (Cont) or ORP10 KO cells showing localization of GFP-EHD1 and endogenous SNX1. Scale bars, 2.5 μm (full size) and 1 μm (inset). **(B)** Quantification of EHD1 fluorescence (Fluo.) at SNX1-positive endosomes (mean ± SEM; n ≥ 10 cells). **(C)** Gallery of representative confocal time-lapse images showing the fission process visualized with GFP-SNX1 in control or ORP10 KO cells. Scale bar, 1 μm. **(D)** Quantification of times required for completion of tubule fission in control (Cont), ORP10 KO cells, ORP10 KO cells rescued by GFP fused to ORP10 (ORP10^{Full}), ΔORD (ORP10^{ΔORD}), or ORP9 (mean ± SEM, the number of fission events for quantification; n = 35 from 11 cells for control, n = 44 from 16 cells for ORP10 KO, n = 33 from 12 cells for ORP10^{Full}, n = 21 from 10 cells for ORP10^{ΔORD}, n = 25 from 10 cells for ORP9). ****, P < 0.0001.

VAPs. Third, ORP10 accommodates and exchanges PI4P and PS at the ER–endosome MCSs. Therefore, we defined ORP10 as a novel lipid exchanger at ER–endosome MCSs.

PI4P- and ORP9-dependent localization of ORP10 at ER–endosome MCSs

We initially identified ORP10 as an endosomal ORP that colocalized with PI4KIIα as well as Rab5, an early endosomal protein. Further investigation revealed that endogenous ORP10 localized more at the later endosomal compartments in addition to Rab5-positive early endosomes. Considering the functional property of ORP10 as a PI4P/PS exchanger at ER–endosome MCSs, the later endosomal localization of this protein is in line with the greater number of ER–endosome MCSs at the later versus early endosomal compartments (Friedman et al., 2013). ORP10 has also been demonstrated to localize at the TGN (Venditti et al., 2019). Because PI4KIIα has been implicated in the generation of a pool of PI4P at the TGN in addition to endosomes (Wang et al., 2003), the localization and function of ORP10 might be under the control of PI4KIIα. In fact, the localization of ORP10 depends

on PI4P, and thus ORP10 would be primarily localized at the PI4P-positive endosomal population. This property fits with the data showing less colocalization with Sac2/INPP5F, an endosomal PI4P phosphatase (Hsu et al., 2015; Nakatsu et al., 2015).

ORP10 associated and colocalized with ORP9 at the ER–endosome MCSs. Such pairing of these proteins at ER–endosome MCSs suggests an interesting possibility of functional coupling. ORP9 has been demonstrated to be a cholesterol transporter (Ngo and Ridgway, 2009). In addition, ORP9 extracts PI4P or cholesterol from liposomes in vitro (Liu and Ridgway, 2014). These studies suggest that ORP9 might have a role as a transporter or exchanger of cholesterol and/or PI4P. Our data showing an increase in endosomal PI4P in ORP9 KO cells (Fig. 5 B) also support this possibility. Given that ORP10 and ORP9 both localize at the same MCSs, both PS and cholesterol would be transported from the ER to endosomes in exchange for PI4P. Because cholesterol has been shown to control the localization and activation of PI4KIIα at endosomes (Minogue et al., 2010; Waugh et al., 2006), ORP9-mediated cholesterol transport at the MCSs would accelerate PI4P production through activation of
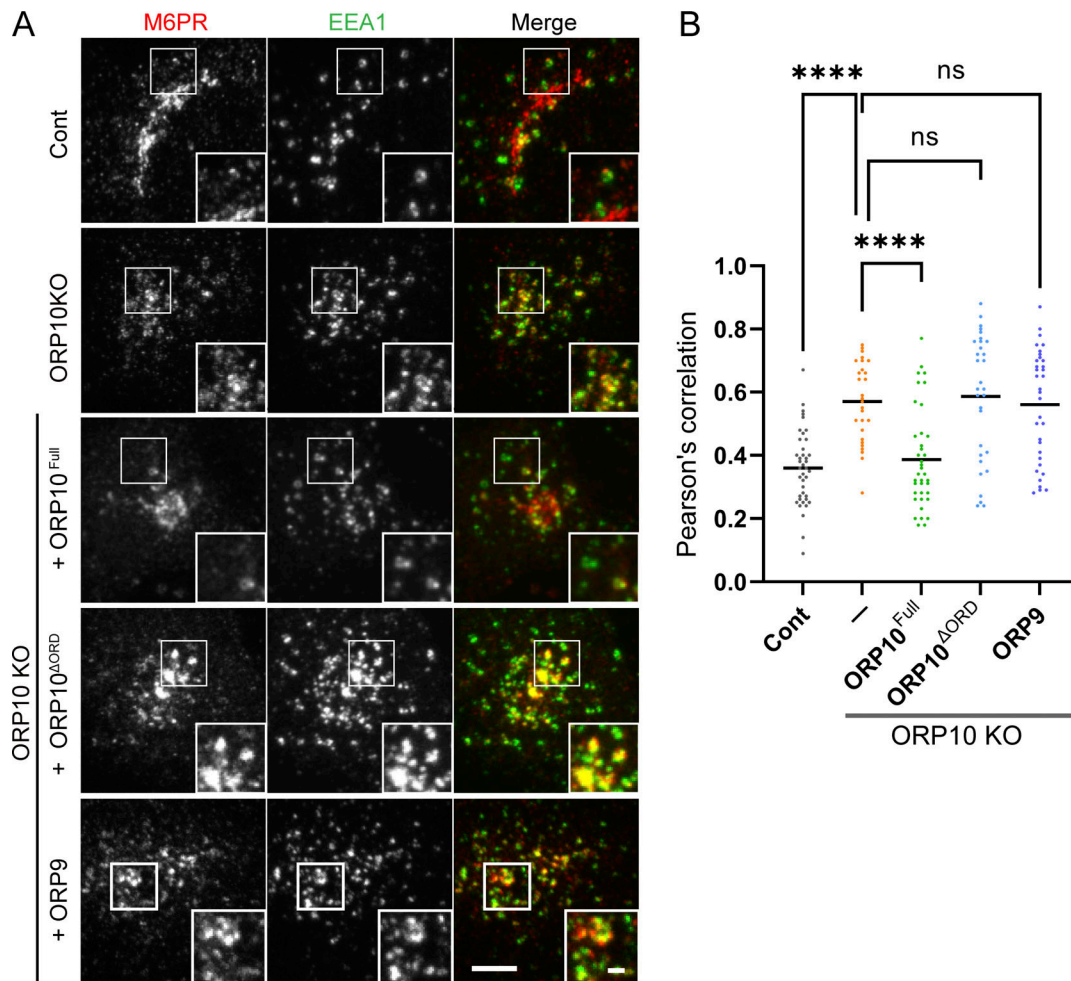
Figure 8. **Accumulation of M6PR in endosomes in ORP10 KO cells. (A)** Immunofluorescence staining of endogenous CI-M6PR and EEA1 in control (Cont), ORP10 KO cells, ORP10 KO cells rescued by GFP fused to ORP10 (ORP10^Full), ΔORD (ORP10^ΔORD), or ORP9. Scale bars, 1 µm (full size) and 1 µm (inset). **(B)** Colocalization analysis of A (mean ± SEM; n ≥ 20 cells). ****, P < 0.0001.

this kinase, which may further promote the localization and function of ORP10 at MCSs. Given that the localization of ORP10 depends on its association with ORP9 in addition to PI4P, one of the major functions of ORP9 may be the control of ORP10 localization at MCSs. Alternatively, a slightly further reduction of endosomal PS levels in ORP9 KO cells (Fig. 5 B) may suggest a possible role of ORP9 as a regulator of endosomal PS itself (via PS transport) or indirectly by regulating other proteins. The role of ORP9 at ER–endosome MCSs will need further investigation.

PI4P/PS exchange by ORP10 as a lipid conversion mechanism on endosomes

Previous studies demonstrated that OSBP and ORP1L localize at the MCSs between the ER and endosomes or phagosomes and control PI4P levels to prevent its accumulation via their transport activity to the ER (Levin-Konigsberg et al., 2019; Dong et al., 2016). These observations suggest a critical importance of the negative regulation of PI4P via its "transport" at these MCSs, although whether lipid countertransport occurred at the ER–endosome MCSs was unknown. We have now demonstrated direct evidence of PI4P/PS exchange by ORP10 at the MCSs

between the ER and endosomes by acute recruitment experiments (Fig. 4, B and C). Furthermore, PS levels on endosomes were reduced in ORP10 KO cells (Fig. 5 B). These gain- and loss-of-function analyses revealed that ORP10 is responsible for the PS supply to endosomes. Therefore, ORP10-mediatd lipid countertransport functions as a nonenzymatic PI4P-to-PS conversion mechanism that enables the reduction of PI4P and the supply of PS at endosomes.

Function of PI4P-to-PS conversion at endosomes mediated by ORP10

Our data suggest that ORP10-mediaed PI4P-to-PS conversion on endosomal membranes promotes EHD1 recruitment and controls the fission of tubulovesicular carriers from endosomes. EHD1, a dynamin-like ATPase, showed an in vitro membrane fission activity that is dependent on its ATPase activity (Deo et al., 2018; Kamerkar et al., 2019). In addition, EHD1 has been shown to be recruited to endosomes by PS and to control retrograde trafficking of cargo proteins, including M6PR (Cullen and Steinberg, 2018; Lee et al., 2015; McKenzie et al., 2012; Seaman, 2012). Thus, ORP10-mediated PI4P/PS conversion may

be directly coupled with the endosome fission process via recruiting EHD1.

From a mechanistic standpoint, ORP10-mediated transport of PS to endosomes via ER–endosome MCSs represents a novel pathway for its delivery to these organelles. However, some PS was still present at endosomes in ORP10 KO cells (Fig. 5 B), suggesting multiple mechanisms for its supply. In fact, ATP8A1, a flippase for phospholipids such as PS and PE (Best et al., 2019; Lee et al., 2015), has been shown to facilitate translocation of PS from the luminal side to the cytoplasmic leaflet of recycling endosome membranes, thereby supporting the localization and function of EHD1 at recycling endosomes in COS-1 cells (Lee et al., 2015). Based on the data (Lee et al., 2015) as well as on previous studies (Gagescu et al., 2000; Vance and Steenbergen, 2005), the amount of PS in the cytosolic leaflet of recycling endosomes has been estimated to be 25–50% of total phospholipids in recycling endosomes. Because the amount of PS in the cytosolic leaflet of recycling endosomes was also not fully depleted in ATP8A1 KD cells (Lee et al., 2015), cells might use two or more independent pathways to provide and/or keep this amount of PS on the cytosolic surface of endosomes for functions such as EHD1 recruitment and cargo trafficking. In addition, ORP10-mediated PS transport occurs upon the formation of MCSs between the ER and endosomes, and thus the timing and/or subendosomal zone for PS transport might be differentially controlled between the two mechanisms in time and space. Another possibility would be a difference in the acyl-chain properties of PS transported by ORP10 or ATP8A1. Considering that ORP10 is able to transport a pool of PS directly from the ER, the site of its synthesis, the ORP10-mediated pathway might be more tunable in terms of acyl-chain quality of PS in addition to its quantity.

It has been demonstrated that ER–endosome MCSs are involved in the regulation of endosome fission (Allison et al., 2017; Phillips and Voeltz, 2016; Raiborg et al., 2015; Rowland et al., 2014). In particular, the importance of actin regulation at ER–endosome MCSs has been demonstrated. Coronin-1c, a regulator of actin disassembly, regulates the formation of ER–endosome MCSs and endosome fission (Hoyer et al., 2018). OSBP, along with VAPs, has also been shown to control actin polymerization at the ER–endosome MCSs, which is closely coupled to the endosome fission process. Dong et al. (2016) reported that in cells lacking OSBP or VAPs, PI4P accumulated at endosomes due to a defect in PI4P transport via MCSs. This in turn caused robust actin polymerization, thereby leading to dysregulation of retromer-mediated membrane trafficking from endosomes. Consistently, loss of ORP10 showed a similar defect in M6PR trafficking observed in OSBP/VAP-null cells, supporting the idea that lipid regulation at ER–endosome MCSs is closely coupled to retrograde membrane trafficking. However, ORP10 KO cells did not show PI4P accumulation or robust actin polymerization, suggesting a distinct regulatory role of PI4P and PS. Given that down-regulation of endosomal PI4P at the ER–endosome MCSs is critical for termination of actin assembly (Dong et al., 2016), ORP10-mediated PI4P-to-PS conversion may simultaneously control actin disassembly and endosome tubule fission by reducing PI4P and supplying PS, respectively, and coordinate those key events on the same membrane.

In sum, our study demonstrates ORP10 as a novel PI4P/PS exchanger at ER–endosome MCSs and the cellular role of ORP10-mediated lipid exchange (Fig. S5). We propose that PI4P-driven lipid countertransport occurs widely at MCSs in cells and serves as a lipid conversion mechanism that may control a variety of biological functions.

Materials and methods
Antibodies and reagents
Primary antibodies used in this study were: mouse antibodies against HA tag, actin, ORP9, VPS35, SNX1, IL-2Rα, and M6PR; rabbit antibodies against GFP, ORP10, EEA1, EHD1, PI4KIIα, and golgin 97; and rat antibodies against HA tag. Alexa Fluor dye–conjugated and HRP-conjugated secondary antibodies were also used in this study (Table S1).

Lipids used in this study were: PC (1,2-dioleoyl-sn-glycero-3-phosphocholine), PI4P (L-α-phosphatidylinositol-4-phosphate [brain, porcine]), PS (L-α-PS [brain, porcine]), Rhod-PE [1,2-dipalmitoyl-sn-glycero-3-phosphoethanolamine-N-(lissamine rhodamine B sulfonyl)], 17:0/14:1 PI [1-heptadecanoyl-2-(9Z-tetradecenoyl)-sn-glycero-3-phospho-(1′-myo-inositol)], 8:0/8:0-PI $[(4,5)P_2(1,2$-dioctanoyl-sn-glycero-3-phospho-(1′-myo-inositol-4′, 5′-bisphosphate)], 17:0/20:4-PI4P [1-heptadecanoyl-2-(5Z,8Z,11Z,14Z-eicosatetraenoyl)-sn-glycero-3-phospho-(1′-myo-inositol-4′-phosphate)], 17:0/20:4-PI(4,5)P_2 [(1-heptadecanoyl-2-(5Z,8Z,11Z, 14Z-eicosatetraenoyl)-sn-glycero-3-phospho-(1′-myo-inositol-4′,5′-bisphosphate)], and 17:0/20:4-PI(3,4,5)P_3 [(1-heptadecanoyl-2-(5Z, 8Z,11Z,14Z-eicosatetraenoyl)-sn-glycero-3-phospho-(1′-myo-inositol-3′, 4′,5′-trisphosphate)] (Avanti Polar Lipids).

Rapamycin (Sigma-Aldrich) was dissolved in DMSO (Sigma-Aldrich), and rhodamine phalloidin (Cytoskeleton, Inc.) was dissolved in methanol (Fujifilm).

siRNAs
For siRNA, 27-mer siRNA duplexes were purchased from Integrated DNA Technologies. The siRNA target sequences were as follows: DS NC1: sense: 5′-CGUUAAUCGCGUAUAAUACGCGUAT-3′; antisense: 5′-AUACGCGUAUUAUACGCGAUUAACGAC-3′; ORP10 siRNA: sense: 5′-AGAUAUUCUCACUUAGUCAACUCCT-3′; antisense: 5′-AGGAGUUGACUAAGUGAGAAUAUCUUU-3′. VAPA siRNA: sense: 5′-AACUAAUGGAAGAGUGUAAAAGA-3′; antisense: 5′-AGUCUUUUACACUCUUCCAUUAGUUUC-3′; VAPB siRNA: sense: 5′-UUAAGAAGGUUAUGGAAGAAUGUAA-3′; antisense: 5′-UCUUACAUUCUUCCAUAACCUUCUUAA-3′; EHD1 siRNA: sense: 5′-GGAGAGAUCUACCAGAAGAUUGAGC-3′; antisense: 5′-GCUCAAUCUUCUGGUAGAUCUCUCCGA-3′.

Plasmids
The plasmids constructed in this study were: AcGFP-ORP10, ORP10-ΔORD-GFP, AcGFP-ORP10-ΔPH, N-term-ORP10-AcGFP, ORP10-PH1-AcGFP, ORP10-PHx2-AcGFP (2xPH^{ORP10}-AcGFP), mCherry-ORP9, BFP-VAPA, mScarlet-rPI4KIIα, 3xFlag-ORD^{ORP10}, GST-ORD^{ORP10}, GST-ORP10$^{268-374}$, GFP-SNX1, GFP-EHD1, Tac-CI-M6PR-tail, ORP9-ΔORD-G4Sx3-AcGFP, PM-FRB-iRFP713, mScarlet-FKBP-ORD^{ORP10}, mScarlet-FKBP-ORD$^{ORP10-HH/AA}$, mScarlet-FKBP-Sac1d$^{Sac2/INPP5F}$, mScarlet-FKBP-MTM1, BFP-FKBP-ORD^{ORP10},

Kawasaki et al.
Lipid exchange by ORP10 regulates endosome fission

Journal of Cell Biology 12 of 19
https://doi.org/10.1083/jcb.202103141

GFP-INPP5F-D460A, HA-ORP9, ORP9-ΔORD-FRB-iRFP, pX330A-1x2 ORP9, pX330A-1x2 ORP10 v1, all-in-one CRISPR-Cas9 vector-ORP10, and CRIS-PITCh(V2)-ORP10. Details of the construction of these plasmids are summarized in Table S2. The sources of the other plasmids purchased or kindly provided were: pEBFP-C1 (Takara), pEGFP-C1 (Takara), pEGFP-N1 (Takara), pAcGFP-C1 (Takara), pAcGFP-N1 (Takara), pmCherry-C1 (Takara), pGEX6P-1 (Cytiva), p3xFLAG-CMV-10 (Sigma-Aldrich), RFP-Sec61β (Tom Rapoport, Harvard Medical School, Boston, MA), GFP-OSBP-PH (Tim Levine, University College London, London, UK), mCherry-2xFyve (Addgene, 140050), GFP-rPI4KIIα (Pietro De Camilli, Yale University, New Haven, CT), iRFP-FRB-Rab5 (Addgene, 51612), iRFP-FRB-Rab7 (Addgene, 51613), GFP-Rab5 (Marino Zerial, Max Planck Institute, Dresden, Germany), GFP-Rab7A (Addgene, 28047), PM-FRB-CFP (Addgene, 67517), mRFP-FKBP12-5ptase domain (Addgene, 67516), mRFP-LactC2 (Addgene, 74061), GFP-BioID-FAM21 (Addgene, 121046), pmScarlet-i-C1 (Addgene, 85044), HA-VAPA (Mitsuo Tagaya, Tokyo University of Pharmacy and Life Sciences, Tokyo, Japan), pX330S-2-PITCh (Addgene, 63670), pX330A-1x2 (Addgene, 58766), pCRIS-PITChv2-FBL (Addgene, 63672), CI-M6PR (GFP fused to the full-length CI-M6PR [G-CIMPR-Full]); Satoshi Waguri, Fukushima Medical University, Fukushima, Japan), GST-LactC2 (Guillaume Drin, Centre national de la recherche scientifique, Valbonne, France), GST–four-phosphate-adaptor protein (FAPP; Guillaume Drin), GST-ORD^{ORP8} (Pietro De Camilli), and Tac-LI (Hiroshi Ohno, RIKEN, Yokohama, Japan).

Protein expression and purification

Purification of GST-tagged ORP10 fragment corresponding to residues 268–374 (GST-ORP10$^{268-374}$) for antibody production was performed using the following protocol. Protein expression was induced in *Escherichia coli* BL21(DE3) transformed with pGEX-GST-ORP10$^{268-374}$ by addition of 0.2 mM IPTG followed by incubation for 24 h at 18°C. Cells were harvested, lysed with 1 mg/ml lysozyme, sonicated in lysis buffer (50 mM Tris-HCl pH 7.5, 300 mM NaCl, 1 mM EDTA, 0.3% Triton X-100, 1 mM DTT, 1 mM PMSF, 1× cOmplete ULTRA EDTA-free [Sigma-Aldrich], and 50 U/ml Benzonase nuclease [Novagen]), and centrifuged at 15,000 rpm for 20 min using a refrigerated high-speed centrifuge (R20A2. Eppendorf Himac). The clear lysate obtained was incubated with glutathione Sepharose 4B resin (Cytiva) for 2 h at 4°C, and then the resin was washed with buffer A (50 mM Tris-HCl, pH 7.5, 300 mM NaCl, 1 mM EDTA, 0.3% Triton X-100, 1 mM DTT, and 0.1 mM PMSF) followed by buffer B (50 mM Tris-HCl, pH 7.5, 1 mM EDTA, 1 mM DTT, 0.3 M NaCl, and 0.1 mM PMSF). The resin was incubated in buffer B containing 2 mM ATP and 5 mM MgCl$_2$ for 30 min at 25°C to reduce nonspecifically bound proteins. The GST tag was cleaved with 50 U/ml PreScission protease (Cytiva) in buffer B on a column for 20 h at 4°C, and the protein was eluted from the resin using buffer B. Residual GST was removed by incubating the eluate with glutathione Sepharose 4B. Flowthrough was concentrated using an Amicon Ultra-4 filter unit (EMD Millipore).

Purification of ORD^{ORP10} or ORD^{ORP8} protein for in vitro lipid transport assay was performed using the following protocol. *E. coli* BL21(DE3) was transformed with the plasmid encoding GST-ORD1$^{ORP10-368-766}$ for expression of ORD^{ORP10} or GST-ORD^{ORP8}

for expression of ORD^{ORP8}. The methods used for protein expression, preparation of bacterial lysate, and GST affinity purification were the same as that for GST-ORP10$^{268-374}$ described above. Following cleavage of GST, the eluate was concentrated using an Amicon Ultra-4 filter unit loaded on a 16/60 Superdex 75 Increase 10/300 GL column (Cytiva) attached to the ÄKTA pure purification system (Cytiva), and the column was developed with buffer GF (50 mM Tris, pH 7.5, 200 mM NaCl, 1 mM EDTA, 5% glycerol, 1 mM DTT, and 0.1 mM PMSF). Peak fractions obtained were pooled, concentrated using the Amicon Ultra-4 filter unit, and frozen in liquid nitrogen.

Purification of the PH domain from FAPP1 (PH^{FAPP}) or the C2 domain from lactadherin (C2^{Lact}) was performed as described previously (Moser von Filseck et al., 2015). *E. coli* BL21(DE3) was transformed with the plasmid encoding GST-PH^{FAPP} or GST-C2^{Lact} (kindly provided by G. Drin). GST-PH^{FAPP} and GST-C2^{Lact} were expressed at 37°C for 4 h upon 1 mM IPTG induction. Cells were harvested, lysed with 1 mg/ml lysozyme, sonicated in lysis buffer (50 mM Tris, pH 7.5, 150 mM NaCl, 1 mM EDTA, 1 mM DTT, 0.1 mM PMSF, 50 U/ml Benzonase nuclease), and centrifuged at 15,000 rpm for 20 min. The obtained supernatant was incubated with glutathione Sepharose 4B resin for 2 h at 4°C. After washing, the resin was incubated with thrombin to cleave GST tag, and the crude eluate was applied on a 16/60 Superdex 75 Increase 10/300 GL column (Cytiva) to obtain PH^{FAPP} or C2^{Lact} protein.

To label PH^{FAPP} or C2^{Lact} protein with NBD, the protein solution was applied on a gel filtration column (NAP-25; GE Healthcare) to remove DTT and then mixed with a 10-fold excess of N,N′-dimethyl-N-(iodoacetyl)-N′-(7-nitrobenz-2-oxa-1,3-diazol-4-yl)ethylenediamine (IANBD-amide; Molecular Probes) for 16 h at 4°C. After stopping the reaction by adding the excess L-cysteine, the free NBD probe was removed by gel filtration. The labeled protein was analyzed by SDS-PAGE and UV spectroscopy. The labeling yield (~100%) was estimated from the ratio of the OD of tyrosine and tryptophan at 280 nm (extinction coefficient ε = 29,450 M/cm for PH^{FAPP}, ε = 45,045 M/cm for C2^{Lact}) and NBD at 495 nm (ε = 25,000 M/cm).

Purification of 3xFLAG-ORD^{ORP10} protein for ligand determination was performed as described below. Expi293F cells (Thermo Fisher Scientific) transfected with the plasmid encoding 3xFlag-ORD^{ORP10} were harvested and lysed in lysis buffer (20 mM Tris-HCl, pH 8.0, containing 150 mM NaCl-halt inhibitor cocktail; Thermo Fisher Scientific) by applying three freeze–thaw cycles. Soluble lysates thus obtained were affinity purified with agarose conjugated with anti-DDDDK-tag antibodies (MBL), and proteins were eluted using an excess amount of FLAG peptide (MBL). The eluted proteins were concentrated and further purified using gel filtration chromatography on a 16/60 Superdex 75 Increase 10/300 GL column (Cytiva) attached to the ÄKTA pure purification system (Cytiva) as described above.

Production of antibody against ORP10

Rabbit ORP10 antiserum was raised against ORP10 fragment corresponding to residues 268–374 (ORP10$^{268-374}$) by Eve Bioscience Co. Ltd. Sera obtained from the final blood samples were diluted, and Western blotting was used to detect human ORP10.

Cell culture and transfection

HeLa (kindly provided by Tomotake Kanki, Niigata University, Niigata, Japan), Cos7 (kindly provided by Pietro De Camilli), or HEK293T (kindly provided by Michiyuki Matsuda, Kyoto University, Kyoto, Japan) cells were maintained at 37°C with 5% CO_2 in DMEM (Fujifilm) supplemented with 10% FBS (Gibco). Plasmids were transfected using either FuGENE HD Transfection Reagent (Promega) or Polyethylenimine Max (Polyscience Inc.) following the manufacturer's instructions. For gene silencing, siRNAs were transiently transfected using Lipofectamine RNAiMAX transfection reagent (Invitrogen). The final concentration of siRNA duplexes was 10 nM. For rapamycin-induced dimerization, cells were incubated with 250 nM rapamycin at 37°C.

CRISPR/Cas9-mediated genome engineering

To establish the ORP10 KO cell line, HeLa cells were co-transfected with a plasmid encoding gRNA for human ORP10 (pX330A-1x2 ORP10 v1) and a plasmid containing puromycin resistance gene using FuGENE HD according to the manufacturer's instructions, and the cells were subjected to puromycin selection 24 h later. Selected cells were plated on 96-well plates at a density of one cell per well. Clones were identified using Sanger sequencing of genomic PCR products and Western blotting using anti-ORP10 antibody.

To establish the ORP9 KO cell line, we used the same protocol used above for ORP10 KO, except a plasmid encoding gRNA for human ORP9 (pX330A-1x2 ORP9) for transfection and anti-ORP9 antibody for Western blotting.

Regarding ORP10-3xHA KI, for endogenous tagging of ORP10 with 3xHA, the CRISPR/Cas9-based PITCh system (Sakuma et al., 2016) was used in this study. HeLa cells were co-transfected with the plasmid encoding Cas9 nuclease, PITCh-gRNA, and ORP10-gRNA (all-in-one CRISPR-Cas9 vector ORP10) and a plasmid for microhomology-mediated DNA repair [CRIS-PITCh(V2)-ORP10]. After 72 h, these cells were subjected to puromycin selection. Selected cells were plated on 96-well plates at a density of one cell per well. Clones were identified using Sanger sequencing of genomic PCR products and Western blotting using anti-HA antibody.

Immunofluorescence microscopy and live-cell imaging

Cells seeded on coverslips coated with polyethyleneimine were fixed for 30 min using 4% PFA on ice, quenched with 50 mM NH_4Cl, permeabilized with blocking buffer (5% normal goat serum, 0.1% saponin in PBS) for 60 min, and incubated with primary antibodies diluted in blocking buffer overnight at 4°C. After five washes with PBS, the cells were incubated with secondary antibodies or rhodamine phalloidin diluted in a blocking buffer for 1 h, followed by five washes with PBS, and mounted on glass slides with ProLong Diamond (Invitrogen). For the anti-Tac antibody uptake assay, HeLa cells transfected with Tac-CI-M6PR-tail were transferred to a well containing ice-cold DH buffer (DMEM supplemented with 20 mM Hepes and 1% FCS) for 15 min. Surface Tac-CI-M6PR-tail was incubated for 30 min in cold DH buffer–containing anti-Tac (anti–IL-2Rα) antibody. The coverslips were washed twice with ice-cold PBS, transferred

to a prewarmed growth medium, and returned to the incubator for 60 min to allow uptake of the antibody. At the endpoint of the assay, the cells were washed, fixed, and immunostained with anti–Golgin 97 antibody and then incubated with fluorescent anti-mouse and anti-rabbit antibodies. For live imaging, transfected cells were seeded on glass-bottomed dishes coated with polyethyleneimine and imaged using Leibovitz's L15 medium (Gibco) supplemented with 10% FBS at 37°C. Fluorescence images were acquired using a confocal laser scanning microscope (FV3000; Olympus) equipped with gallium arsenide phosphide detectors (two-channel high-sensitivity spectral detector and two-channel spectral detector), an incubation chamber (IX83HB; TOKAI HIT), and a 100× oil objective lens (1.4 NA, UPlanSAPO; Olympus).

Image analysis

Confocal images were analyzed using Fiji and CellSens (Olympus). For colocalization studies, Pearson's correlation (measuring correlation in variations between two channels) was measured using the method of Costes to set automatic thresholds. For image deconvolution, CellSens Dimension software version 2.1 (Olympus) was used. A constrained iterative 3D deconvolution module with advanced maximum likelihood estimation algorithm was employed. For quantification of GFP-SNX1–positive endosomal tubule fission (Fig. 7), tubules (defined as linear structures having a length >1 µm) were measured. The number of fission events for quantification of times required for completion of tubule fission was as follows: $n = 35$ from 11 cells for control, $n = 44$ from 16 cells for ORP10 KO, $n = 33$ from 12 cells for ORP10^{Full}, $n = 21$ from 10 cells for ORP10$^{\Delta ORD}$, $n = 25$ from 10 cells for ORP9. For quantification of the traffic of Tac-CI-M6PR (Fig. 6), images were subjected to background correction, and the internalized fluorescence intensity of Tac-CI-M6PR was measured by manually selecting an area covering the whole cell. Vesicular fluorescence intensity was obtained by subtracting fluorescence intensity in the Golgi complex from total fluorescence intensity. Data are presented as vesicular/Golgi fluorescence ratio from each cell ($n \geq 6$ cells). For quantification of endosomal PI4P and PS probes (Fig. 4 B), cells were transfected with GFP-OSBP-PH or mCherry-LactC2, and the vesicles containing fluorescent signals, which were confirmed to colocalize with PI4KIIα in a separate experiment, were manually selected (region of interest [ROI]). Mean fluorescence pixel intensity in the ROI was calculated and normalized by the mean fluorescence pixel intensity of the background (cytoplasm) to adjust for differences in expression levels ($n = 11$ cells). For quantification of endosomal PI4P and PS levels (Fig. 5, B and C), control, ORP10 KO, or ORP9 KO cells were transfected with GFP-OSBP-PH or mCherry-LactC2, and the vesicles containing fluorescent signals were manually selected (ROI). Mean fluorescence pixel intensity in the ROI was calculated and normalized by the mean fluorescence pixel intensity of the background (cytoplasm) to adjust for differences in expression levels. The number of endosomes for PS quantification in Fig. 5 B was as follows: $n = 136$ from 11 cells for control, $n = 131$ from 17 cells for ORP10 KO, $n = 112$ from 13 cells for ORP9 KO. The number of endosomes for PI4P quantification in Fig. 5 B was as follows: $n = 168$ from 20 cells for

control, n = 157 from 21 cells for ORP10 KO, n = 149 from 17 cells for ORP9 KO. The number of endosomes for PS quantification in Fig. 5 C was as follows: n = 78 from 35 cells for GFP, n = 145 from 17 cells for ORP10^{Full}, n = 90 from 11 cells for ORP10$^{\Delta ORD}$, n = 73 from 10 cells for ORP10$^{\Delta PH}$, n = 120 from 12 cells for ORP9. For quantification of EHD1 on SNX1-positive endosomes (Fig. 7 A and Fig. S4 A), cells were immunostained with antibodies against EHD1 and SNX1, or cells transfected with GFP-EHD1 were subjected to immunofluorescence staining with anti-SNX1 antibody. SNX1-positive endosomes were marked as the ROI, and the fluorescence intensities of endogenous EHD1 or GFP-EHD1 were measured in each ROI. Mean fluorescence pixel intensity in the ROI was calculated and normalized using the mean fluorescence pixel intensity of the background to adjust for differences in expression levels (n ≥ 10 cells). To quantify the colocalization of M6PR and EEA1 (Fig. 8, A and B), Pearson's correlation (measuring the correlation between two channels) was measured (n ≥ 20 cells).

Acute phosphoinositide depletion by the rapamycin-based FKBP/FRB dimerization system
Cells expressing GFP-2xFyve, GFP-OSBP-PH, 2xPH^{ORP10}-AcGFP or AcGFP-ORP10, mScarlet-FKBP-MTM1 or mScarlet-FKBP-Sac1d$^{Sac2/INPP5F}$, and iRFP-FRB-Rab5 or iRFP-FRB-Rab7 were imaged before and after the addition of 250 nM rapamycin. For quantification of PI3P, PI4P, PH^{ORP10}, and ORP10 probes on endosomes, endosomes containing iRFP signals were marked as the ROI, and the fluorescence intensities of GFP-2xFyve, GFP-OSBP-PH, 2xPH^{ORP10}-AcGFP, or AcGFP-ORP10 were measured in each ROI, respectively (Sac1d$^{Sac2/INPP5F}$ recruitment for 2xPH^{ORP10}, n = 11 cells; MTM1 recruitment for 2xPH^{ORP10}, n = 11 cells; Sac1d$^{Sac2/INPP5F}$ recruitment for OSBP-PH, n = 9 cells; MTM1 recruitment for 2xPHFyve, n = 11 cells; Sac1d$^{Sac2/INPP5F}$ recruitment for GFP-ORP10, n = 7 cells).

In situ lipid exchange assay
Cos7 cells expressing GFP-OSBP-PH or mCherry-LactC2, BFP-FKBP-ORP10-ORD, ORP9-ΔORD-FRB-iRFP, and HA-VAPB were imaged before and after the addition of 250 nM rapamycin. For quantification of PI4P and PS probes on endosomes tethered to ER by ORP9-ΔORD-FRB-iRFP/VAPA, endosomes containing iRFP signals were marked as the ROI, and the fluorescence intensities of GFP-OSBP-PH or mCherry-LactC2 were measured in each ROI (n = 11 cells).

Liposome preparations
Lipids were mixed in a glass vial and dried to form a film under a stream of N_2 gas. After further drying in a vacuum for 1 h, the lipid film was rehydrated in 50 mM Hepes, pH 7.2, 120 mM potassium acetate (HK buffer). The suspension was processed by applying five freeze–thaw cycles and extruded through a polycarbonate filter (pore size 200 nm) using a miniextruder (Avanti Polar Lipids). Liposomes were stored at 4°C and in the dark when containing fluorescent lipids and used within 48 h.

In vitro lipid transport assay
An in vitro lipid transport assay was performed as previously described (Moser von Filseck et al., 2015) with slight modifications.

For the PI4P transport assay, donor liposome L_B (200 µM total lipids) containing 2% Rhod-PE and 4% PI4P in HKM (HK + 1 mM MgCl$_2$) buffer solution was mixed with NBD-PH^{FAPP} at a final concentration of 250 nM. The accessible PI4P concentration in the outer leaflet of liposome membranes was 4 µM. Then, 1 min later, acceptor liposome L_A (200 µM total lipids) composed of only PC or PC + 5% PS was mixed to make a transport assay mixture. An aliquot was immediately transferred to a well (100 µl/well, total of 3 wells for triplicate measurements) in a 96-well plate, and the fluorescence measurements were started. After 3 min, purified ORD (either ORP8 or ORP10) was mixed with the rest of the assay mixture at a final concentration of 200 nM, and then an aliquot was immediately transferred to the other well (100 µl/well, total of 3 wells for triplicate measurements) in the same 96-well plate for fluorescence measurement. The NBD fluorescence, which reflects the transport of PI4P to acceptor liposome L_A, was measured with a Tecan SPARK every 15 s with the following measurement parameters/conditions: excitation at 460 nm (5-nm bandwidth), emission at 530 nm (10-nm bandwidth), vigorous shaking every 15 s, temperature 30°C. To determine the amount of PI4P transported to liposome L_A by ORD protein, we normalized the NBD fluorescence as follows. We measured the NBD fluorescence (F_{eq}) that corresponds to a situation where PI4P is fully equilibrated between liposomes (by maximum transport). NBD-PH^{FAPP} (250 nM) was mixed with liposome L_A and L_B (200 µM total lipid each) with a lipid composition similar to that of liposomes used for the transport assay, except that each contains 2% PI4P. The fraction of PI4P in the outer leaflet of liposome L_B, PI4P$_B$/PI4P$_{Total}$, was equal to the fraction of PH^{FAPP} on liposome L_B and corresponded to F_{Norm} = $0.5 \times (F - F_0/F_{eq} - F_0)$ with F_0 corresponding to the NBD fluorescence before the addition ORD protein. The amount of PI4P (in µM) transported to liposome L_A corresponds to $4 \times F_{Norm}$. Three independent experiments were performed in triplicate.

For the PS transport assay, donor liposome L_A (200 µM total lipids) containing 2% Rhod-PE and 5% PS in HKM buffer solution was mixed with NBD-C2^{Lact} at a final concentration of 250 nM. The accessible PS concentration in the outer leaflet of liposome membranes was 5 µM. Then, 1 min later, we mixed acceptor liposome L_B (200 µM total lipids) composed of only PC or PC + 4% PI4P to make a transport assay mixture. An aliquot was immediately transferred to a well (100 µl/well, total of three wells for triplicate measurements) in a 96-well plate, and the fluorescence measurements were started. After 3 min, purified ORD (either ORP8 or ORP10) was mixed with the rest of the assay mixture at a final concentration of 200 nM, and then an aliquot was immediately transferred to the other well (100 µl/well, total of three wells for triplicate measurements) in the same 96-well plate for fluorescence measurement. The NBD fluorescence, which reflects the transport of PS to liposome L_B, was measured with a Tecan SPARK as described above for PI4P transport assay. To determine the amount of PS transported to liposome L_B by ORD protein, we normalized the NBD fluorescence with a similar method for that of PI4P described above. Namely, we measured the NBD fluorescence (F_{eq}) that corresponds to a situation where PS is fully equilibrated between liposomes (by maximum transport). NBD-C2^{Lact} (250 nM)

was mixed with liposome L_A and L_B (200 µM total lipid each) with a lipid composition similar to that of liposomes used for the transport assay, except that each contained 2.5% PS. The fraction of PS in the outer leaflet of L_A liposome, PS_A/PS_{Total}, was equal to the fraction of C2^{Lact} on liposome L_A and corresponded to $F_{Norm} = 0.5 \times (F - F_0/F_{eq} - F_0)$, with F_0 corresponding to the NBD fluorescence before the addition ORD protein. The amount of PS (in µM) transported to liposome L_B corresponded to $5 \times F_{Norm}$. Three independent experiments were performed in triplicate.

Coimmunoprecipitation
HEK293T cells were transfected with plasmids using Polyethylenimine Max. Cells were lysed in immunoprecipitation buffer (50 mM Tris-HCl, 0.5% NP-40, 1 mM PMSF, 1× cOmplete ULTRA EDTA-free [Sigma-Aldrich], and PhosSTOP [Sigma-Aldrich]) 24 h after transfection. The lysates thus obtained were centrifuged at 13,000 ×g for 15 min at 4°C, and the supernatants were incubated with anti-GFP antibody and protein G Mag Sepharose (Cytiva) for 1 h at 4°C. Beads were washed three times with the immunoprecipitation buffer, and the bound proteins were eluted in an SDS-PAGE sample buffer. The eluates were loaded onto a 10% acrylamide gel for SDS-PAGE followed by immunoblotting.

Identification of ORP10-binding protein(s)
For immunoprecipitation, parental control cells or ORP10 3xHA KI HeLa cells were lysed in immunoprecipitation buffer (20 mM Hepes-KOH, pH 7.5, 150 mM NaCl, 0.1% Triton X-100, 1× cOmplete ULTRA EDTA-free [Sigma-Aldrich], and phosphatase inhibitor [Fujifilm]) and subjected to immunoprecipitation using anti-HA magnetic beads (Thermo Fisher Scientific). The beads were washed twice with 10 mM Hepes-KOH, pH 7.5, containing 150 mM NaCl and 0.1% Triton X-100 and eluted with 100 mM glycine, pH 2.0. The eluates were subjected to TCA precipitation. Precipitated proteins were pelleted using centrifugation and washed with acetone. The protein pellets were solubilized in 0.1 M ammonium bicarbonate, pH 8.8, containing 0.05% decyl β-D-glucopyranoside, reduced using 5 mM tris(2-carboxyethyl) phosphine (Thermo Fisher Scientific), and subsequently alkylated using 10 mM iodoacetamide. After alkylation, the samples were digested using lysyl-endopeptidase (Fujifilm) for 3 h at 37°C, followed by N-p-Tosyl-L-phenylalanine chloromethyl ketone (Sigma-Aldrich) for 12 h at 37°C.

For MS, digested samples were analyzed using a nanoscale liquid chromatography–tandem MS (LC-MS/MS) system as previously described (Natsume et al., 2002). The peptide mixture was applied to a Mightysil-PR-18 (Kanto Chemical) fritless column (45 × 0.150–mm inner diameter) and separated using a 0–40% gradient of acetonitrile containing 0.1% formic acid for 80 min at a flow rate of 100 nl/min. Eluted peptides were sprayed directly into a Triple TOF 5600+ system (SCIEX). MS and MS/MS spectra were obtained using the information-dependent acquisition mode. Up to 25 precursor ions above an intensity threshold of 50 counts/s were selected for MS/MS analyses from each survey scan. All the MS/MS spectra were searched against protein sequences of the National Center for Biotechnology Information nonredundant human protein dataset (NCBInr RefSeq Release 71, containing 179,460 entries)

using the Protein Pilot software package (SCIEX). Protein quantification was performed using the intensity-based absolute quantification method (Schwanhäusser et al., 2011) without conversion to absolute amounts using universal proteomics standards (iBQ). The iBQ value was calculated by dividing the sum of the ion intensities of all the identified peptides of each protein by the number of theoretically measurable peptides.

Ligand determination for ORP10
Sample preparation for LC-MS/MS for phosphatidylinositol phosphates (PIPs)
Purified 3xFlag-ORD^{ORP10} proteins were mixed with 700 µl of methanol containing C8:0/C8:0 PI(4,5)P$_2$ to prevent adsorption of phosphoinositides on glassware. After addition of the surrogate internal standard mixture containing C17:0/C14:1-PI, C17:0/C20:4-PI3P, C17:0/C20:4-PI4P, C17:0/C20:4-PI5P, C17:0/C20:4-PI(3,4)P$_2$, C17:0/C20:4-PI(3,5)P$_2$, 17:0/20:4-PI(4,5)P$_2$, and 17:0/20:4-PI(3,4,5)P$_3$ at 10 pmol each, the samples were subjected to lipid extraction with methanol: 2 M HCl:chloroform (1:2:4). The organic phase was loaded onto a diethylaminoethylcellulose column (Santa Cruz Biotechnology), which was washed sequentially with 3 ml of chloroform:methanol (1:1) and 2 ml of chloroform:methanol:saturated (28%) ammonia:glacial acetic acid (200:100:3:0.9), followed by 1.5 ml chloroform:methanol:12 M HCl:water (12:12:1:1) to elute acidic phospholipids. After a methylation reaction according to the method proposed by Clark et al. (2011), the derivatives were dried under a stream of N$_2$ gas, and the residues were dissolved in 36 µl of methanol/70% ethylamine/water (100:0.065:33).

MS for PIPs
LC-MS/MS was performed with an LC system connected to a triple-stage quadrupole mass spectrometer (QTRAP 6500; SCIEX). We used a new HPLC-MS method (unpublished data) to analyze C32:0; C32:1; C34:0; C34:1; C34:2; C36:0; C36:1; C36:2, C36:3; C36:4; C38:3; C38:4; C38:5; C38:6; C40:4; C40:5; C40:6 species of phosphoinositides in the immunoprecipitates, and the combined total of all species measured is presented in Figs. 3 A and S2 A. Amounts of the species in each class were calculated based on those of the class-matched C31:1 PI or C37:4 phosphoinositides added to the samples as surrogate internal standards before lipid extraction and methylation procedures.

Statistics and reproducibility
All data are presented as the mean ± SEM. GraphPad Prism 4 (GraphPad Software) was used for statistical analysis. The two-tailed t test was used to evaluate statistical significance between two groups of samples. For multiple comparison analyses, one-way ANOVA followed by Tukey's least significant difference multiple comparison test was used. $P < 0.05$ was considered statistically significant.

Online supplemental material
Fig. S1 shows the localization of ORP10 at endosomes and the ER–endosome MCSs. Fig. S2 shows the ORD^{ORP10} ligand and its lipid countertransport activity. Fig. S3 shows acute recruitment

of ORD^{ORP10} to ER–endosome MCSs. Fig. S4 shows EHD1 and other regulators for retrograde membrane trafficking at endosomes in ORP10 KO cells. Fig. S5 shows schematic summary for ORP10-medated lipid countertransport and its role in retrograde membrane trafficking. Table S1 shows the antibodies used in this study. Table S2 shows the plasmids constructed in this study. Video 1 shows endosome fission in a control HeLa cell. Video 2 shows endosome fission in an ORP10 KO HeLa cell.

Acknowledgments

References

Alli-Balogun, G.O., and T.P. Levine. 2019. Regulation of targeting determinants in interorganelle communication. *Curr. Opin. Cell Biol.* 57:106–114. https://doi.org/10.1016/j.ceb.2018.12.010

Allison, R., J.R. Edgar, G. Pearson, T. Rizo, T. Newton, S. Günther, F. Berner, J. Hague, J.W. Connell, J. Winkler, et al. 2017. Defects in ER–endosome contacts impact lysosome function in hereditary spastic paraplegia. *J. Cell Biol.* 216:1337–1355. https://doi.org/10.1083/jcb.201609033

Antonny, B., J. Bigay, and B. Mesmin. 2018. The oxysterol-binding protein cycle: burning off PI(4)P to transport cholesterol. *Annu. Rev. Biochem.* 87: 809–837. https://doi.org/10.1146/annurev-biochem-061516-044924

Arighi, C.N., L.M. Hartnell, R.C. Aguilar, C.R. Haft, and J.S. Bonifacino. 2004. Role of the mammalian retromer in sorting of the cation-independent mannose 6-phosphate receptor. *J. Cell Biol.* 165:123–133. https://doi.org/10.1083/jcb.200312055

Baba, T., D.J. Toth, N. Sengupta, Y.J. Kim, and T. Balla. 2019. Phosphatidylinositol 4,5-bisphosphate controls Rab7 and PLEKHM1 membrane cycling during autophagosome–lysosome fusion. *EMBO J.* 38:e100312. https://doi.org/10.15252/embj.2019102837

Balla, A., and T. Balla. 2006. Phosphatidylinositol 4-kinases: old enzymes with emerging functions. *Trends Cell Biol.* 16:351–361. https://doi.org/10.1016/j.tcb.2006.05.003

Balla, A., G. Tuymetova, M. Barshishat, M. Geiszt, and T. Balla. 2002. Characterization of type II phosphatidylinositol 4-kinase isoforms reveals association of the enzymes with endosomal vesicular compartments. *J. Biol. Chem.* 277:20041–20050. https://doi.org/10.1074/jbc.M111807200

Balla, A., G. Tuymetova, A. Tsiomenko, P. Várnai, and T. Balla. 2005. A plasma membrane pool of phosphatidylinositol 4-phosphate is generated by phosphatidylinositol 4-kinase type-III alpha: studies with the PH domains of the oxysterol binding protein and FAPP1. *Mol. Biol. Cell.* 16:1282–1295. https://doi.org/10.1091/mbc.e04-07-0578

Balla, T., Y.J. Kim, A. Alvarez-Prats, and J. Pemberton. 2019. Lipid dynamics at contact sites between the endoplasmic reticulum and other organelles. *Annu. Rev. Cell Dev. Biol.* 35:85–109. https://doi.org/10.1146/annurev-cellbio-100818-125251

Best, J.T., P. Xu, and T.R. Graham. 2019. Phospholipid flippases in membrane remodeling and transport carrier biogenesis. *Curr. Opin. Cell Biol.* 59: 8–15. https://doi.org/10.1016/j.ceb.2019.02.004

Blondeau, F., J. Laporte, S. Bodin, G. Superti-Furga, B. Payrastre, and J.L. Mandel. 2000. Myotubularin, a phosphatase deficient in myotubular myopathy, acts on phosphatidylinositol 3-kinase and phosphatidylinositol 3-phosphate pathway. *Hum. Mol. Genet.* 9:2223–2229. https://doi.org/10.1093/oxfordjournals.hmg.a018913

Bohnert, M. 2020. Tether me up, tether me in—dynamic organelle contact sites in metabolic rewiring. *Dev. Cell.* 54:212–225. https://doi.org/10.1016/j.devcel.2020.06.026

Bonifacino, J.S., and R. Rojas. 2006. Retrograde transport from endosomes to the trans-Golgi network. *Nat. Rev. Mol. Cell Biol.* 7:568–579. https://doi.org/10.1038/nrm1985

Burd, C., and P.J. Cullen. 2014. Retromer: a master conductor of endosome sorting. *Cold Spring Harb. Perspect. Biol.* 6:a016774. https://doi.org/10.1101/cshperspect.a016774

Burke, J.E. 2018. Structural basis for regulation of phosphoinositide kinases and their involvement in human disease. *Mol. Cell.* 71:653–673. https://doi.org/10.1016/j.molcel.2018.08.005

Chung, J., F. Torta, K. Masai, L. Lucast, H. Czapla, L.B. Tanner, P. Narayanaswamy, M.R. Wenk, F. De Camilli. 2015. PI4P/phosphatidylserine countertransport at ORP5- and ORP8-mediated ER–plasma membrane contacts. *Science.* 349:428–432. https://doi.org/10.1126/science.aab1370

Clark, J., K.E. Anderson, V. Juvin, T.S. Smith, F. Karpe, M.J.O. Wakelam, L.R. Stephens, and P.T. Hawkins. 2011. Quantification of PtdInsP3 molecular species in cells and tissues by mass spectrometry. *Nat. Methods.* 8: 267–272. https://doi.org/10.1038/nmeth.1564

Cullen, P.J., and F. Steinberg. 2018. To degrade or not to degrade: mechanisms and significance of endocytic recycling. *Nat. Rev. Mol. Cell Biol.* 19: 679–696. https://doi.org/10.1038/s41580-018-0053-7

D'Souza, R.S., J.Y. Lim, A. Turgut, K. Servage, J. Zhang, K. Orth, N.G. Sosale, M.J. Lazzara, J. Allegood, and J.E. Casanova. 2020. Calcium-stimulated disassembly of focal adhesions mediated by an ORP3/IQSec1 complex. *eLife.* 9:e54113. https://doi.org/10.7554/eLife.54113

de Saint-Jean, M., V. Delfosse, D. Douguet, G. Chicanne, B. Payrastre, W. Bourguet, B. Antonny, and G. Drin. 2011. Osh4p exchanges sterols for phosphatidylinositol 4-phosphate between lipid bilayers. *J. Cell Biol.* 195: 965–978. https://doi.org/10.1083/jcb.201104062

Del Bel, L.M., and J.A. Brill. 2018. Sac1, a lipid phosphatase at the interface of vesicular and nonvesicular transport. *Traffic.* 19:301–318. https://doi.org/10.1111/tra.12554

Deo, R., M.S. Kushwah, S.C. Kamerkar, N.Y. Kadam, S. Dar, K. Babu, A. Srivastava, and T.J. Pucadyil. 2018. ATP-dependent membrane remodeling links EHD1 functions to endocytic recycling. *Nat. Commun.* 9:5187. https://doi.org/10.1038/s41467-018-07586-z

Derivery, E., C. Sousa, J.J. Gautier, B. Lombard, D. Loew, and A. Gautreau. 2009. The Arp2/3 activator WASH controls the fission of endosomes through a large multiprotein complex. *Dev. Cell.* 17:712–723. https://doi.org/10.1016/j.devcel.2009.09.010

Dong, R., Y. Saheki, S. Swarup, L. Lucast, J.W. Harper, and P. De Camilli. 2016. Endosome–ER contacts control actin nucleation and retromer function through VAP-dependent regulation of PI4P. *Cell.* 166:408–423. https://doi.org/10.1016/j.cell.2016.06.037

Friedman, J.R., J.R. Dibenedetto, M. West, A.A. Rowland, and G.K. Voeltz. 2013. Endoplasmic reticulum–endosome contact increases as endosomes traffic and mature. *Mol. Biol. Cell.* 24:1030–1040. https://doi.org/10.1091/mbc.e12-10-0733

Gagescu, R., N. Demaurex, R.G. Parton, W. Hunziker, L.A. Huber, and J. Gruenberg. 2000. The recycling endosome of Madin-Darby canine

kidney cells is a mildly acidic compartment rich in raft components. *Mol. Biol. Cell.* 11:2775–2791. https://doi.org/10.1091/mbc.11.8.2775

Gautreau, A., K. Oguievetskaia, and C. Ungermann. 2014. Function and regulation of the endosomal fusion and fission machineries. *Cold Spring Harb. Perspect. Biol.* 6:a016832. https://doi.org/10.1101/cshperspect.a016832

Ghai, R., X. Du, H. Wang, J. Dong, C. Ferguson, A.J. Brown, R.G. Parton, J.-W. Wu, and H. Yang. 2017. ORP5 and ORP8 bind phosphatidylinositol-4, 5-biphosphate (PtdIns(4,5)P $_2$) and regulate its level at the plasma membrane. *Nat. Commun.* 8:757. https://doi.org/10.1038/s41467-017-00861-5

Gillooly, D.J., I.C. Morrow, M. Lindsay, R. Gould, N.J. Bryant, J.M. Gaullier, R.G. Parton, and H. Stenmark. 2000. Localization of phosphatidylinositol 3-phosphate in yeast and mammalian cells. *EMBO J.* 19:4577–4588. https://doi.org/10.1093/emboj/19.17.4577

Gomez, T.S., and D.D. Billadeau. 2009. A FAM21-containing WASH complex regulates retromer-dependent sorting. *Dev. Cell.* 17:699–711. https://doi.org/10.1016/j.devcel.2009.09.009

Grant, B.D., and S. Caplan. 2008. Mechanisms of EHD/RME-1 protein function in endocytic transport. *Traffic.* 9:2043–2052. https://doi.org/10.1111/j.1600-0854.2008.00834.x

Hammond, G.R.V., M.P. Machner, and T. Balla. 2014. A novel probe for phosphatidylinositol 4-phosphate reveals multiple pools beyond the Golgi. *J. Cell Biol.* 205:113–126. https://doi.org/10.1083/jcb.201312072

Holthuis, J.C.M., and A.K. Menon. 2014. Lipid landscapes and pipelines in membrane homeostasis. *Nature.* 510:48–57. https://doi.org/10.1038/nature13474

Hoyer, M.J., P.J. Chitwood, C.C. Ebmeier, J.F. Striepen, R.Z. Qi, W.M. Old, and G.K. Voeltz. 2018. A novel class of ER membrane proteins regulates ER-associated endosome fission. *Cell.* 175:254–265.e14. https://doi.org/10.1016/j.cell.2018.08.030

Hsu, F., F. Hu, and Y. Mao. 2015. Spatiotemporal control of phosphatidylinositol 4-phosphate by Sac2 regulates endocytic recycling. *J. Cell Biol.* 209:97–110. https://doi.org/10.1083/jcb.201408027

Huotari, J., and A. Helenius. 2011. Endosome maturation. *EMBO J.* 30: 3481–3500. https://doi.org/10.1038/emboj.2011.286

Kamerkar, S.C., K. Roy, S. Bhattacharyya, and T.J. Pucadyil. 2019. A screen for membrane fission catalysts identifies the ATPase EHD1. *Biochemistry.* 58:65–71. https://doi.org/10.1021/acs.biochem.8b00925

Kentala, H., M. Weber-Boyvat, and V.M. Olkkonen. 2016. OSBP-related protein family: mediators of lipid transport and signaling at membrane contact sites. *Int. Rev. Cell Mol. Biol.* 321:299–340. https://doi.org/10.1016/bs.ircmb.2015.09.006

Lee, S., Y. Uchida, J. Wang, T. Matsudaira, T. Nakagawa, T. Kishimoto, K. Mukai, T. Inaba, T. Kobayashi, R.S. Molday, et al. 2015. Transport through recycling endosomes requires EHD1 recruitment by a phosphatidylserine translocase. *EMBO J.* 34:669–688. https://doi.org/10.15252/embj.201489703

Lemmon, M.A. 2008. Membrane recognition by phospholipid-binding domains. *Nat. Rev. Mol. Cell Biol.* 9:99–111. https://doi.org/10.1038/nrm2328

Levin-Konigsberg, R., F. Montaño-Rendón, T. Keren-Kaplan, R. Li, B. Ego, S. Mylvaganam, J.E. DiCiccio, W.S. Trimble, M.C. Bassik, J.S. Bonifacino, et al. 2019. Phagolysosome resolution requires contacts with the endoplasmic reticulum and phosphatidylinositol-4-phosphate signalling. *Nat. Cell Biol.* 21:1234–1247. https://doi.org/10.1038/s41556-019-0394-2

Levine, T.P., and S. Munro. 2002. Targeting of Golgi-specific pleckstrin homology domains involves both PtdIns 4-kinase-dependent and -independent components. *Curr. Biol.* 12:695–704. https://doi.org/10.1016/S0960-9822(02)00779-0

Lipp, N.-F., S. Ikhlef, J. Milanini, and G. Drin. 2020. Lipid exchangers: cellular functions and mechanistic links with phosphoinositide metabolism. *Front. Cell Dev. Biol.* 8:663. https://doi.org/10.3389/fcell.2020.00663

Liu, X., and N.D. Ridgway. 2014. Characterization of the sterol and phosphatidylinositol 4-phosphate binding properties of Golgi-associated OSBP-related protein 9 (ORP9). *PLoS One.* 9:e108368. https://doi.org/10.1371/journal.pone.0108368

Loewen, C.J.R., A. Roy, and T.P. Levine. 2003. A conserved ER targeting motif in three families of lipid binding proteins and in Opi1p binds VAP. *EMBO J.* 22:2025–2035. https://doi.org/10.1093/emboj/cdg201

Maeda, K., K. Anand, A. Chiapparino, A. Kumar, M. Poletto, M. Kaksonen, and A.-C. Gavin. 2013. Interactome map uncovers phosphatidylserine transport by oxysterol-binding proteins. *Nature.* 501:257–261. https://doi.org/10.1038/nature12430

McKenzie, J.E., B. Raisley, X. Zhou, N. Naslavsky, T. Taguchi, S. Caplan, and D. Sheff. 2012. Retromer guides STxB and CD8-M6PR from early to recycling endosomes, EHD1 guides STxB from recycling endosome to Golgi. *Traffic.* 13:1140–1159. https://doi.org/10.1111/j.1600-0854.2012.01374.x

Mellman, I. 1996. Endocytosis and molecular sorting. *Annu. Rev. Cell Dev. Biol.* 12:575–625. https://doi.org/10.1146/annurev.cellbio.12.1.575

Mesmin, B., and B. Antonny. 2016. The counterflow transport of sterols and PI4P. *Biochim. Biophys. Acta.* 1861:940–951. https://doi.org/10.1016/j.bbalip.2016.02.024

Mesmin, B., J. Bigay, J. Moser von Filseck, S. Lacas-Gervais, G. Drin, and B. Antonny. 2013. A four-step cycle driven by PI(4)P hydrolysis directs sterol/PI(4)P exchange by the ER-Golgi tether OSBP. *Cell.* 155:830–843. https://doi.org/10.1016/j.cell.2013.09.056

Mesmin, B., J. Bigay, J. Polidori, D. Jamecna, S. Lacas-Gervais, and B. Antonny. 2017. Sterol transfer, PI4P consumption, and control of membrane lipid order by endogenous OSBP. *EMBO J.* 36:3156–3174. https://doi.org/10.15252/embj.201796687

Minogue, S., K.M.E. Chu, E.J. Westover, D.F. Covey, J.J. Hsuan, and M.G. Waugh. 2010. Relationship between phosphatidylinositol 4-phosphate synthesis, membrane organization, and lateral diffusion of PI4KIIα at the trans-Golgi network. *J. Lipid Res.* 51:2314–2324. https://doi.org/10.1194/jlr.M005751

Moser von Filseck, J., A. Čopič, V. Delfosse, S. Vanni, C.L. Jackson, W. Bourguet, and G. Drin. 2015. Phosphatidylserine transport by ORP/Osh proteins is driven by phosphatidylinositol 4-phosphate. *Science.* 349: 432–436. https://doi.org/10.1126/science.aab1346

Nakatsu, F., and A. Kawasaki. 2021. Functions of oxysterol-binding proteins at membrane contact sites and their control by phosphoinositide metabolism. *Front. Cell Dev. Biol.* 9:664788. https://doi.org/10.3389/fcell.2021.664788

Nakatsu, F., M. Messa, R. Nández, H. Czapla, Y. Zou, S.M. Strittmatter, and P. De Camilli. 2015. Sac2/INPP5F is an inositol 4-phosphatase that functions in the endocytic pathway. *J. Cell Biol.* 209:85–95. https://doi.org/10.1083/jcb.201409064

Naslavsky, N., and S. Caplan. 2011. EHD proteins: key conductors of endocytic transport. *Trends Cell Biol.* 21:122–131. https://doi.org/10.1016/j.tcb.2010.10.003

Natsume, T., Y. Yamauchi, H. Nakayama, T. Shinkawa, M. Yanagida, N. Takahashi, and T. Isobe. 2002. A direct nanoflow liquid chromatography-tandem mass spectrometry system for interaction proteomics. *Anal. Chem.* 74:4725–4733. https://doi.org/10.1021/ac020018n

Ngo, M., and N.D. Ridgway. 2009. Oxysterol binding protein-related protein 9 (ORP9) is a cholesterol transfer protein that regulates Golgi structure and function. *Mol. Biol. Cell.* 20:1388–1399. https://doi.org/10.1091/mbc.e08-09-0905

Nguyen, P.M., N.R. Gandasi, B. Xie, S. Sugahara, Y. Xu, and O. Idevall-Hagren. 2019. The PI(4)P phosphatase Sac2 controls insulin granule docking and release. *J. Cell Biol.* 218:3714–3729. https://doi.org/10.1083/jcb.201903121

Nissilä, E., Y. Ohsaki, M. Weber-Boyvat, J. Perttilä, E. Ikonen, and V.M. Olkkonen. 2012. ORP10, a cholesterol binding protein associated with microtubules, regulates apolipoprotein B-100 secretion. *Biochim. Biophys. Acta.* 1821:1472–1484. https://doi.org/10.1016/j.bbalip.2012.08.004

Phillips, M.J., and G.K. Voeltz. 2016. Structure and function of ER membrane contact sites with other organelles. *Nat. Rev. Mol. Cell Biol.* 17:69–82. https://doi.org/10.1038/nrm.2015.8

Pietrangelo, A., and N.D. Ridgway. 2018. Bridging the molecular and biological functions of the oxysterol-binding protein family. *Cell. Mol. Life Sci.* 75:3079–3098. https://doi.org/10.1007/s00018-018-2795-y

Prinz, W.A., A. Toulmay, and T. Balla. 2020. The functional universe of membrane contact sites. *Nat. Rev. Mol. Cell Biol.* 21:7–24. https://doi.org/10.1038/s41580-019-0180-9

Puthenveedu, M.A., B. Lauffer, P. Temkin, R. Vistein, P. Carlton, K. Thorn, J. Taunton, O.D. Weiner, R.G. Parton, and M. von Zastrow. 2010. Sequence-dependent sorting of recycling proteins by actin-stabilized endosomal microdomains. *Cell.* 143:761–773. https://doi.org/10.1016/j.cell.2010.10.003

Raiborg, C., E.M. Wenzel, and H. Stenmark. 2015. ER–endosome contact sites: molecular compositions and functions. *EMBO J.* 34:1848–1858. https://doi.org/10.15252/embj.201591481

Raychaudhuri, S., and W.A. Prinz. 2010. The diverse functions of oxysterol-binding proteins. *Annu. Rev. Cell Dev. Biol.* 26:157–177. https://doi.org/10.1146/annurev.cellbio.042308.113334

Rowland, A.A., P.J. Chitwood, M.J. Phillips, and G.K. Voeltz. 2014. ER contact sites define the position and timing of endosome fission. *Cell.* 159: 1027–1041. https://doi.org/10.1016/j.cell.2014.10.023

Sakuma, T., S. Nakade, Y. Sakane, K.T. Suzuki, and T. Yamamoto. 2016. MMEJ-assisted gene knock-in using TALENs and CRISPR-Cas9 with the

PITCh systems. *Nat. Protoc.* 11:118–133. https://doi.org/10.1038/nprot.2015.140

Schwanhäusser, B., D. Busse, N. Li, G. Dittmar, J. Schuchardt, J. Wolf, W. Chen, and M. Selbach. 2011. Global quantification of mammalian gene expression control. *Nature.* 473:337–342. https://doi.org/10.1038/nature10098

Scorrano, L., M.A. De Matteis, S. Emr, F. Giordano, G. Hajnóczky, B. Kornmann, L.L. Lackner, T.P. Levine, L. Pellegrini, K. Reinisch, et al. 2019. Coming together to define membrane contact sites. *Nat. Commun.* 10: 1287. https://doi.org/10.1038/s41467-019-09253-3

Seaman, M.N.J. 2012. The retromer complex – endosomal protein recycling and beyond. *J. Cell Sci.* 125:4693–4702. https://doi.org/10.1242/jcs.103440

Sohn, M., M. Korzeniowski, J.P. Zewe, R.C. Wills, G.R.V. Hammond, J. Humpolickova, L. Vrzal, D. Chalupska, V. Veverka, G.D. Fairn, et al. 2018. PI(4,5)P$_2$ controls plasma membrane PI4P and PS levels via ORP5/8 recruitment to ER-PM contact sites. *J. Cell Biol.* 217:1797–1813. https://doi.org/10.1083/jcb.201710095

Tong, J., H. Yang, H. Yang, S.H. Eom, and Y.J. Im. 2013. Structure of Osh3 reveals a conserved mode of phosphoinositide binding in oxysterol-binding proteins. *Structure.* 21:1203–1213. https://doi.org/10.1016/j.str.2013.05.007

Tong, J., M.K. Manik, H. Yang, and Y.J. Im. 2016. Structural insights into nonvesicular lipid transport by the oxysterol binding protein homologue family. *Biochim. Biophys. Acta.* 1861:928–939. https://doi.org/10.1016/j.bbalip.2016.01.008

Vance, J.E., and R. Steenbergen. 2005. Metabolism and functions of phosphatidylserine. *Prog. Lipid Res.* 44:207–234. https://doi.org/10.1016/j.plipres.2005.05.001

Venditti, R., L.R. Rega, M.C. Masone, M. Santoro, E. Polishchuk, D. Sarnataro, S. Paladino, S. D'Auria, A. Varriale, V.M. Olkkonen, et al. 2019. Molecular determinants of ER–Golgi contacts identified through a new FRET-FLIM system. *J. Cell Biol.* 218:1055–1065. https://doi.org/10.1083/jcb.201812020

Wang, Y.J., J. Wang, H.Q. Sun, M. Martinez, Y.X. Sun, E. Macia, T. Kirchhausen, J.P. Albanesi, M.G. Roth, and H.L. Yin. 2003. Phosphatidylinositol 4 phosphate regulates targeting of clathrin adaptor AP-1 complexes to the Golgi. *Cell.* 114:299–310. https://doi.org/10.1016/S0092-8674(03)00603-2

Waugh, M.G., S. Minogue, D. Chotai, F. Berditchevski, and J.J. Hsuan. 2006. Lipid and peptide control of phosphatidylinositol 4-kinase IIα activity on Golgi-endosomal rafts. *J. Biol. Chem.* 281:3757–3763. https://doi.org/10.1074/jbc.M506527200

Wong, L.H., A.T. Gatta, and T.P. Levine. 2019. Lipid transfer proteins: the lipid commute via shuttles, bridges and tubes. *Nat. Rev. Mol. Cell Biol.* 20:85–101. https://doi.org/10.1038/s41580-018-0071-5

Wu, H., P. Carvalho, and G.K. Voeltz. 2018. Here, there, and everywhere: the importance of ER membrane contact sites. *Science.* 361:eaan5835. https://doi.org/10.1126/science.aan5835

Wyles, J.P., and N.D. Ridgway. 2004. VAMP-associated protein-A regulates partitioning of oxysterol-binding protein-related protein-9 between the endoplasmic reticulum and Golgi apparatus. *Exp. Cell Res.* 297:533–547. https://doi.org/10.1016/j.yexcr.2004.03.052

Yeung, T., G.E. Gilbert, J. Shi, J. Silvius, A. Kapus, and S. Grinstein. 2008. Membrane phosphatidylserine regulates surface charge and protein localization. *Science.* 319:210–213. https://doi.org/10.1126/science.1152066
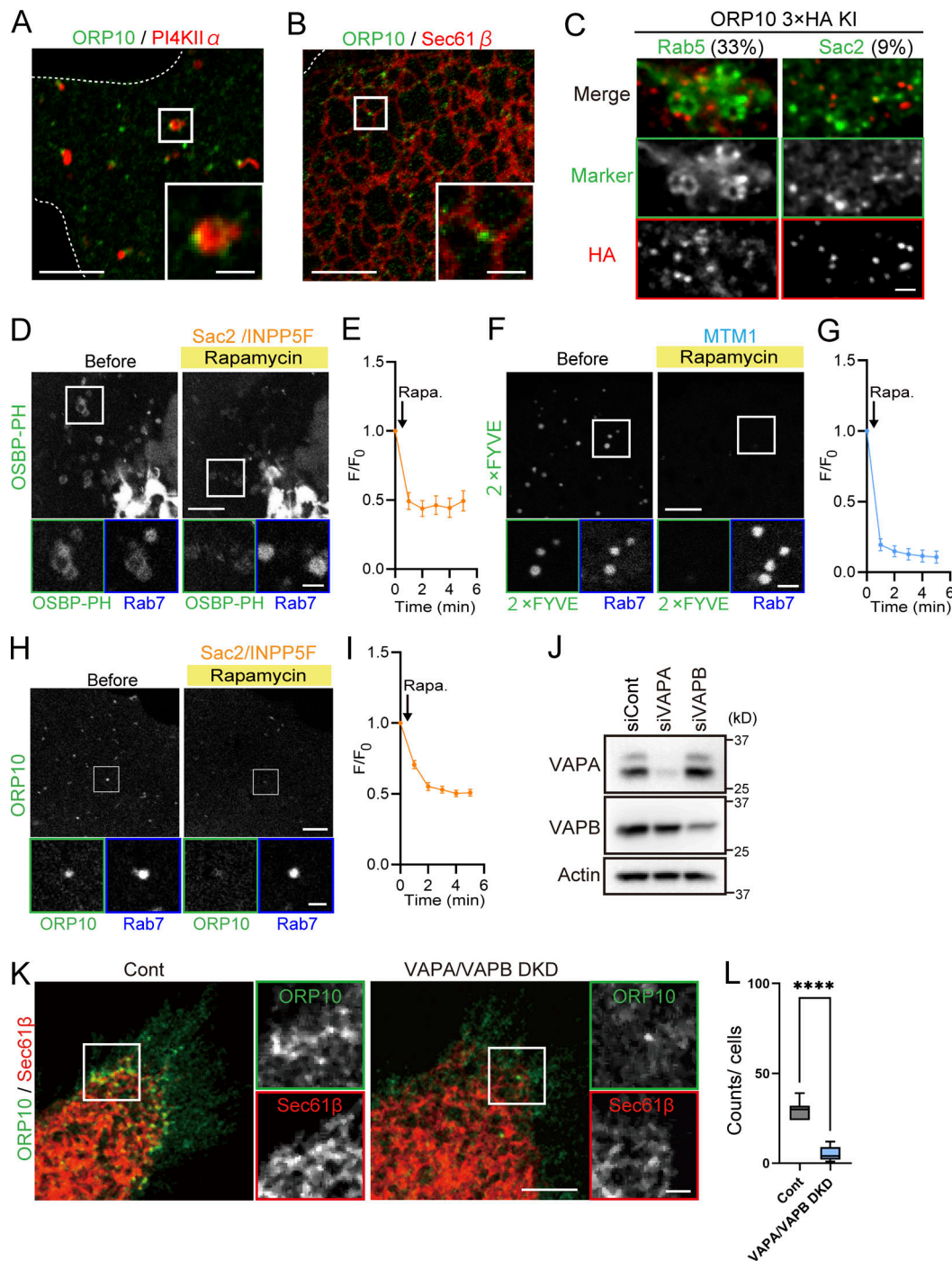
Figure S1. **Localization of ORP10 at endosomes and the ER–endosome MCSs. (A and B)** Representative images of Cos7 cells expressing GFP-ORP10 and mScarlet-PI4KIIα (A) or RFP-Sec61β (B). Scale bars, 5 µm (full size) and 1 µm (inset). **(C)** Colocalization of endogenous ORP10 (ORP10-3xHA) with Rab5 (GFP-Rab5) or Sac2 (GFP-INPP5F-D460A) and its quantification (percentage colocalization; n ≥ 10 cells). Scale bar, 1 µm. **(D and E)** Representative images showing endosomal localization of OSBP PH domain (OSBP-PH) before (0 min) or after (5 min) addition of rapamycin (Rapa.) to recruit FKBP fused with Sac1 domain from Sac2/INPP5F by Rab7-FRB (D) and its kinetics (E; mean ± SEM; n = 9 cells). Scale bars, 5 µm (full size) and 1 µm (inset). **(F and G)** Representative images showing endosomal localization of HRS Fyve domain (2xFYVE) before (0 min) or after (5 min) addition of rapamycin to recruit FKBP fused with MTM1 by Rab7-FRB (F) and its kinetics (G; mean ± SEM; n = 11 cells). Scale bars, 5 µm (full size) and 1 µm (inset). **(H and I)** Representative images showing endosomal localization of ORP10 before (0 min) or after (5 min) recruitment of FKBP fused with Sac1 domain from Sac2/INPP5F by FRB-Rab7 (H) and its kinetics (I; mean ± SEM; n = 7 cells). Scale bars, 5 µm (full size) and 1 µm (inset). **(J)** Western blotting of cells transfected with siRNA for control (siCont), VAPA (siVAPA), or VAPB (siVAPB) by antibodies indicated. **(K and L)** Localization of AcGFP-ORP10 in control (Cont) or VAPA/VAPB double-KD (DKD) cells (K) and its quantification (the number of ORP10-positive endosomal structures associated with the ER). In L, n = 11 cells for control, n = 11 cells for VAPA/B DKD. Scale bars, 5 µm (full size) and 1 µm (inset). ****, P < 0.0001.
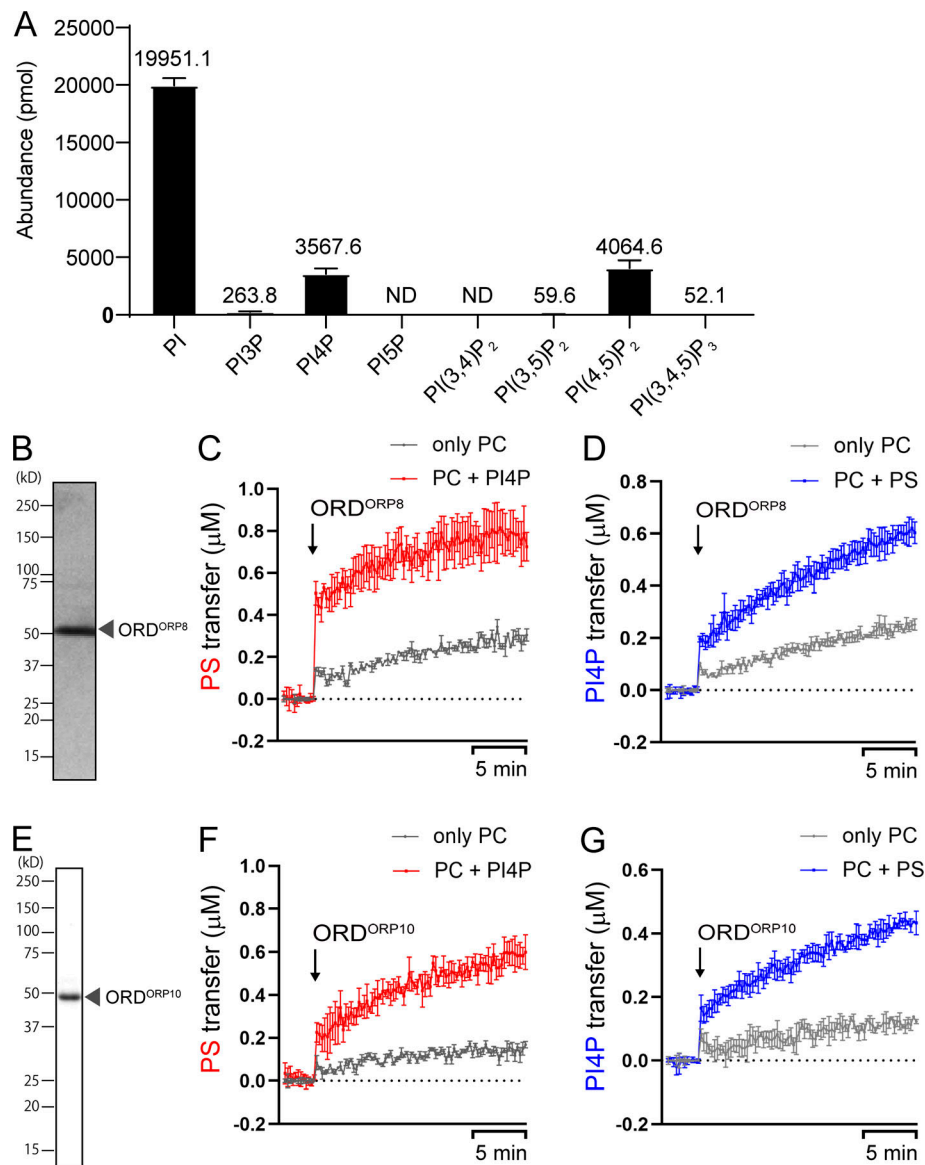
Figure S2. **ORD^{ORP10} ligand and its lipid countertransport activity. (A)** Phosphoinositide species in Expi293F cells (10^7 cells) detected by MS (mean ± SEM; $n = 3$ independent experiments). **(B)** Coomassie Brilliant Blue–stained SDS-PAGE gel of ORD^{ORP8} proteins purified from *E. coli*. **(C)** Kinetic curves of transport of PS (µM) to acceptor liposomes doped with only PC (gray) or PC + PI4P (red) by ORD^{ORP8}. **(D)** Kinetic curves of transport of PI4P (µM) to acceptor liposomes doped with only PC (gray) or PC + PS (blue) by ORD^{ORP8}. **(E)** Coomassie Brilliant Blue–stained SDS-PAGE gel of ORD^{ORP10} proteins purified from *E. coli*. **(F)** Kinetic curves of transport of PS (µM) to acceptor liposomes doped with only PC (gray) or PC + PI4P (red) by ORD^{ORP10}. **(G)** Kinetic curves of transport of PI4P (µM) to acceptor liposomes doped with only PC (gray) or PC + PS (blue) by ORD^{ORP10} (mean ± SD; $n = 3$ independent experiments).
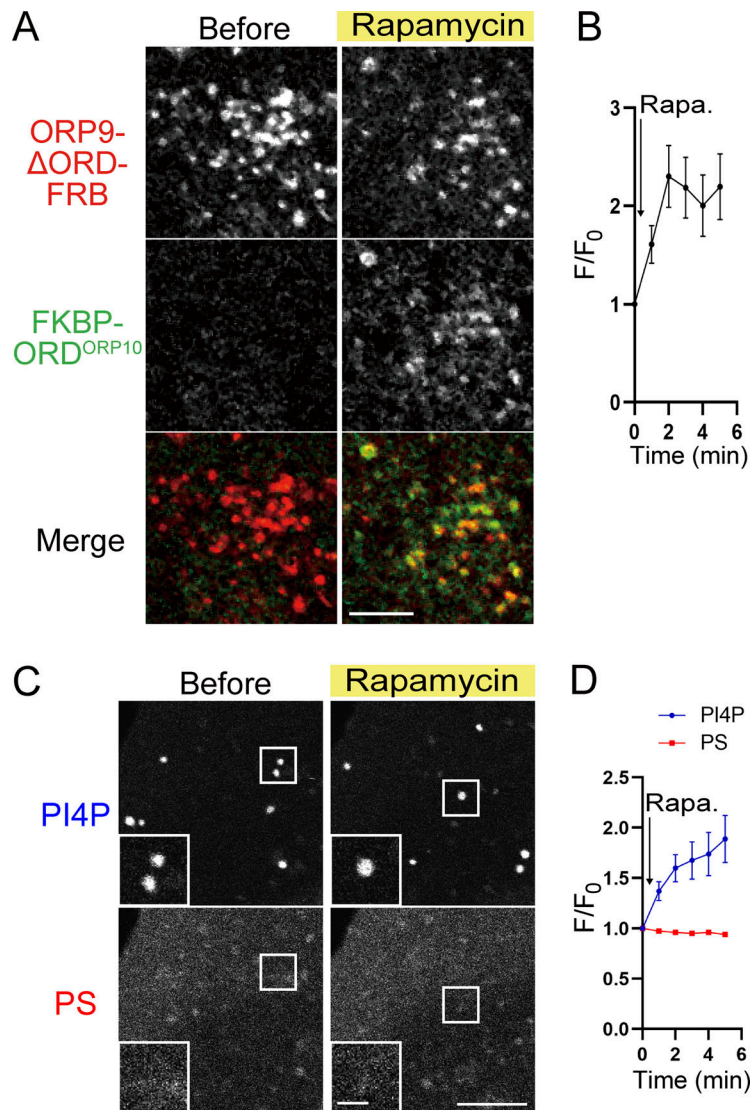
Figure S3. **Acute recruitment of ORD^{ORP10} to ER–endosome MCSs. (A and B)** Live-cell confocal microscopic images showing acute recruitment of mScarlet-FKBP-ORD^{ORP10} from cytosol (0 min) to the ER–endosome MCSs tethered by ORP9-ΔORD-FRB-iRFP (5 min) upon addition of 250 nM rapamycin (Rapa.; A) and its kinetics (B; mean ± SEM; *n* = 11 cells). Scale bar, 5 µm. **(C and D)** Representative snapshot images of confocal live microscopy showing PI4P levels (GFP-OSBP-PH; upper) or PS levels (mRFP-LactC2; lower) before (0 min) and after (5 min) acute recruitment of ORD$^{ORP10-HHAA}$ to ER–endosome MCSs (C) and its quantification (D; mean ± SEM; *n* = 11 cells). Scale bars, 5 µm (full size) and 1 µm (inset).
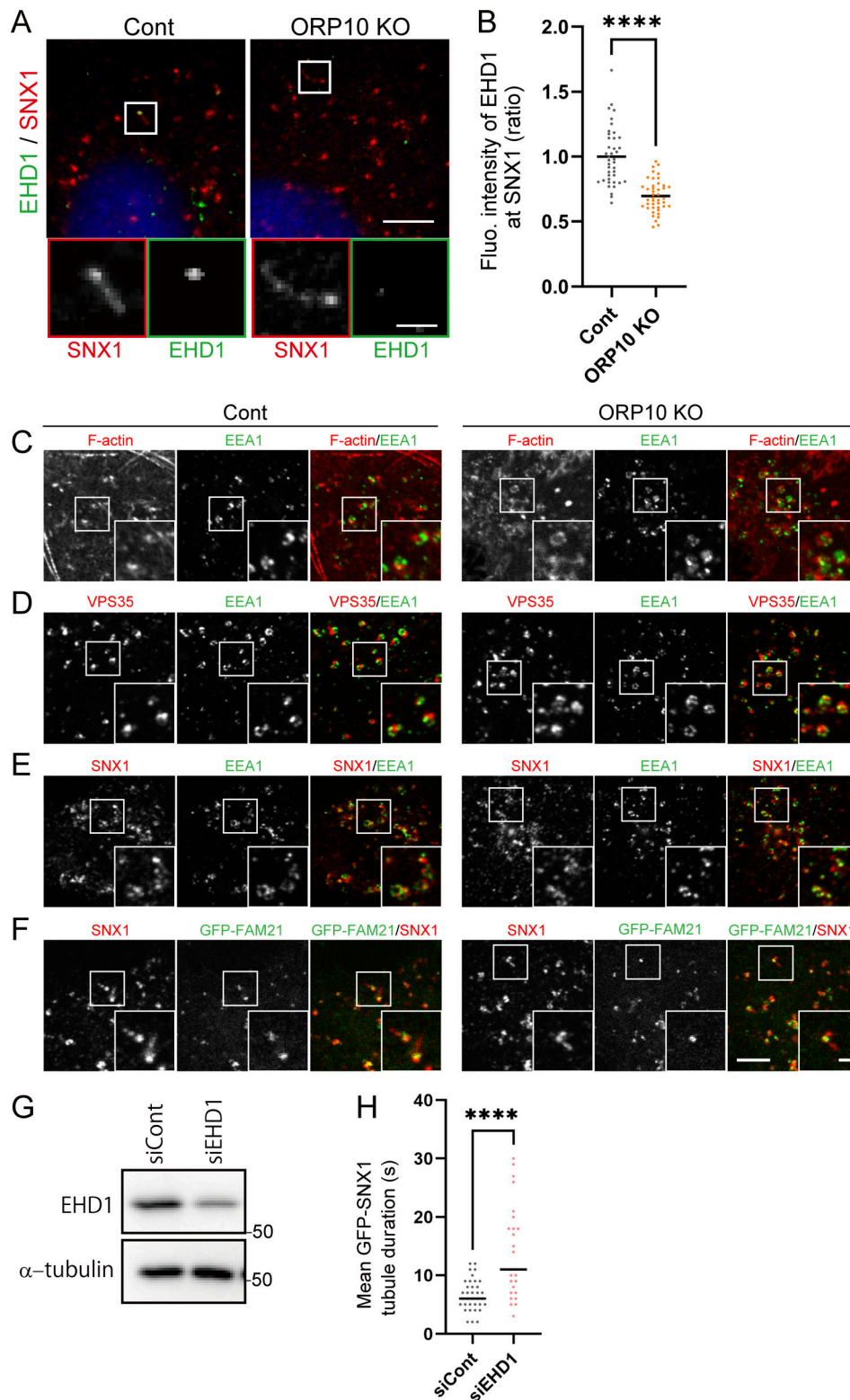
Figure S4. **EHD1 and other regulators for retrograde membrane trafficking at endosomes in ORP10 KO cells. (A)** Confocal microscopic images of control (Cont) or ORP10 KO cells showing localization of endogenous EHD1 and SNX1. Scale bars, 5 μm (full size) and 1 μm (inset). **(B)** Quantification of EHD1 fluorescence (Fluo.) at SNX1-positive endosomes shown in A (mean ± SEM; n = 40 cells). **(C–F)** Representative immunofluorescence images of endogenous EEA1 and F-actin (C), VPS35 (D), or SNX1 (E), and endogenous SNX1 and transiently expressed GFP-FAM21 (F) in control (Cont) or ORP10 KO HeLa cells. Scale bars, 5 μm (full size) and 1 μm (inset). **(G)** Western blotting of cells transfected with siRNA for control (siCont) or EHD1 (siEHD1-1) by antibodies as indicated. **(H)** Quantification of times required for completion of tubule fission in cells transfected with siRNA for control (siCont) or EHD1 (siEHD1-1; mean ± SEM; n = 35 fission events from 11 cells for control, n = 26 fission events from 13 cells for EHD1 KD). ****, P < 0.0001.
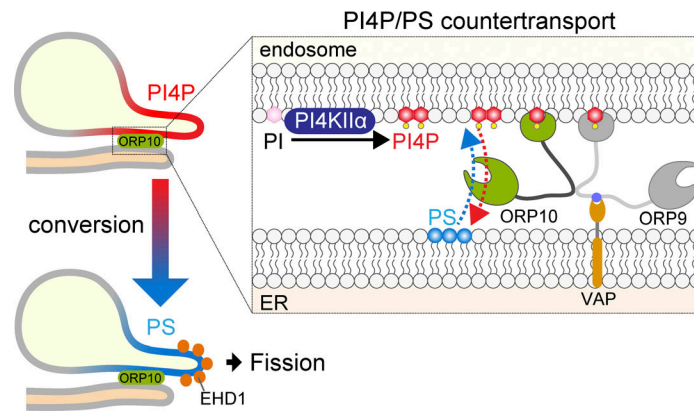
Figure S5. **Schematic summary for ORP10-medated lipid countertransport and its role in retrograde membrane trafficking.** PI4KIIα-mediated PI4P production at endosomes leads to MCS formation by ORP10, ORP9, and VAP. ORP10 mediates countertransport of PI4P and PS at the ER–endosome MCSs, which results in conversion of PI4P to PS at endosomes. A pool of PS then recruits EHD1, a dynamin-like ATPase, at endosomes, thereby promoting endosome fission during retrograde trafficking. See text for details.

Table S1 and Table S2 are provided online as separate Word files. Table S1 shows the antibodies used in this study. Table S2 shows the plasmids constructed in this study.

Kawasaki et al.
Lipid exchange by ORP10 regulates endosome fission

Journal of Cell Biology   S6
https://doi.org/10.1083/jcb.202103141